

Further Steps in LES-Based Noise Prediction for Complex Jets

Michael L. Shur*

“New Technologies and Services” (NTS), St.-Petersburg 197198, Russia

Philippe R. Spalart†

Boeing Commercial Airplanes, Seattle, WA 98124, USA

Michael Kh. Strelets‡

“New Technologies and Services” (NTS), St.-Petersburg 197198, Russia

and

Andrey V. Garbaruk§

St.-Petersburg State Polytechnic University, St.-Petersburg 195220, Russia

The paper presents the status of a CFD/CAA numerical system developed by this team starting in 2001. The aim is to predict the noise from jets of airliner engines with an accuracy of 2-3 dB over a meaningful range of frequencies, while having no empiricism and a general-geometry capability. The first part of the paper outlines the system itself and some results of its testing (a full-length description is given in a recent two-part paper^{1,2}), and the second part presents the latest developments and achievements. These include: an accurate algorithm for shock capturing in LES based on local automatic activation of flux-limiters; a two-step RANS-LES approach to complex nozzles; and a set of simulations of cold and heated jets from round and beveled single nozzles, sonic jets with shocks, jets from dual nozzles (co-planar and staggered, in still air and in co-flowing flow), dual nozzles with fan-flow deflecting vanes, and chevron nozzles. Although all the simulations were carried out on PC clusters with a maximum of six processors and on rather modest grids (2-4 million nodes), in most cases the system is close to the 2-3 dB target accuracy both in terms of directivity and spectrum, albeit limited in terms of frequency (to a diameter Strouhal number that ranges from 2 to 4 depending on the grid used and flow regime). The overall message of the paper is that available CFD/CAA numerical and physical models, if properly combined, are capable of predicting the noise of rather complex jets with quite affordable computational resources and already today can be helpful in a rapid low-cost analysis of different noise-reduction concepts.

I. Introduction

IN engineering practice, the prediction of noise from jet engines is still based on empirical methods and scaling laws such as Lighthill's or, at most, on steady Reynolds-Averaged-Navier-Stokes computations combined with *ad hoc* models for noise sources. The empirical basis of the methods and extreme simplifications of the turbulence responsible for noise generation appear to rule them out as a trustworthy tool for the evaluation of new concepts of noise reduction. Such a tool must deal with many non-trivial features, like wide temperature differences, two-stream flows, imperfectly expanded supersonic streams, jets in co-flowing stream (in flight), non-circular

* Leading Research Scientist, mshur@rscac.spb.ru, Senior Member AIAA.

† Technical Fellow, P.O. Box 3707, philippe.r.spalart@boeing.com.

‡ Principal Scientist, strelets@mail.rcom.ru.

§ Associate Professor, Department of Aerodynamics and Thermodynamics, agarbaruk@rscac.spb.ru.

nozzles, *etc.*, and must be capable of accounting for the subtle effects of design innovations on the turbulent structures responsible for the noise.

These considerations, increasing computing power, and advancing algorithms are the factors driving the field towards LES, the only turbulence-resolving approach feasible at high Reynolds numbers. The application of LES to jet-noise prediction is under way in many research groups now (see the references in Ref.1 and the latest publications³⁻¹²). However most of the studies are more “academic” than “industrial” in that they deal with simple round jets (many of codes lacking general-geometry capabilities) and very few of the “complicating factors” mentioned above. This is partly explained by the extreme demands on the numerical system in order to resolve multiple turbulent scales and by the complexity of combining turbulence and far-field acoustics. Boosting the usefulness of the method therefore means eliminating any waste of computing effort. This highlights the importance of a number of decisions needed for LES-based noise computation, both in the turbulence-simulation and the sound-extraction approaches. LES brings up options for: the configuration of the computational domain and topology of the grid; the numerical scheme and boundary conditions; the Subgrid-Scale (SGS) model (if any); the approach to obtaining transition to turbulence, *etc.* For noise extraction, decisions are needed on using direct or integral methods and, for the latter, a Kirchhoff or Ffowcs-Williams/Hawkings (FWH) formulation, the shape and position of control surfaces, their treatment near the downstream end, *etc.* All these decisions should be assessed not only separately but as an aggregate as well. An analysis of the state of the art¹ shows that the range of approaches being explored is wide, and that the CFD/CAA community is still far from a consensus on the most efficient one. This is fairly normal, considering the complexity of the problem.

In this paper, an overview is presented of the non-empirical numerical system developed by the authors over the last 5 years with the final goal of predicting the noise of engine jets within 2-3dB accuracy over as wide frequency range as possible. The approach seems to combine sensibly some elements of the techniques used in the literature with some new ones and, based on the results obtained so far, is rather promising and has a chance to become a reliable industrial tool, although many physical and numerical characteristics can yet be improved.

The levels of accuracy and geometry completeness reached are, of course, still not sufficient for airliner certification, and will not be for many years, especially as far as the high frequency noise is concerned. However the extrapolation from laboratory experiments to a certification also has its uncertainties, and flow measurements capable of “explaining” the success or failure of a device are essentially impossible, whereas LES provides the entire flow and sound fields. Therefore, the present value of the method lies in helping a more educated, rapid, and low-cost evaluation of noise-reduction devices. The boosted understanding of the flow physics will also, sooner or later, lead to an invention.

The rest of the paper is organized as follows. In Section II a brief overview is presented of the numerical system and major previous results. Then, in Section III a detailed presentation is given of the latest methodological developments (Section III.A) and recent applications (Section III.B). Finally the conclusion section summarizes major achievements and outlines still-unresolved problems.

II. Overview of the Numerical System and Key Previous Results

A detailed description of the numerical approach is presented in two journal articles^{1,2}, along with a set of tests supporting the key elements of the strategy. Briefly, the salient features of the system and “strategic choices” made in LES and noise computation are as follows.

We use the NTS code (Ref.13), which runs on structured multi-block curvilinear grids with implicit 2nd order time integration and dual time stepping. The inviscid differencing is based on the flux-difference splitting scheme of Roe¹⁴. It is a weighted average of 4th-order centered and 5th-order upwind-biased schemes (with typical weights 0.75 and 0.25 respectively) in the turbulent region and acoustic near-field, and “pure” upwind-biased outside that region. The outer boundary conditions are non-reflecting; in addition, a buffer layer is implemented near the outflow.

For the turbulence simulation, our current choice is to de-activate the SGS model and to rely on the subtle numerical dissipation of the slightly upwind scheme, which is compatible with the spirit of LES away from walls. This choice is dictated mostly by the crucial importance of a realistic representation of the transition to turbulence in the jet shear layers, which should be provided by a CFD approach for purposes of noise prediction. This representation is inevitably approximate, since resolving the fine-scale turbulent structures of the nozzle boundary layers that seed the shear layer and cause its rapid transition in the real high-Re jets is far out of reach. Other LES strategies that were tested turned out visibly less successful. If the SGS model is activated, the transition to turbulence is crucially delayed. If only the upwind-biased (3rd or 5th order) schemes are used, the delay also is very pronounced, due to more dissipative numerics¹. Artificial inflow forcing, as employed in many other jet studies,

could resolve this issue to some extent, but was rejected to avoid the creation of parasitic noise and the introduction of a number of arbitrary parameters.

For noise prediction, we use the far-field formulation of the permeable Ffowcs-Williams/Hawkings surface integral method without external quadrupoles, which seems to be the best compromise between efficiency and accuracy. In contrast to the Kirchhoff approach, which could be the other practical option, it allows the placement of the majority of the control surface in the immediate vicinity of the turbulent region (in the inviscid but non-linear near-field) and, therefore, the confinement of the fine-grid area needed for turbulence resolution exactly to this turbulent area. Although the coarsening of the grid does need to be very gradual, the rest of the grid is essentially a “cushion” which absorbs outgoing waves better than a tightly-fitted numerical boundary condition would.

The best shapes for the FWH surfaces around a jet are tapered funnels; this minimizes the loss of quality of the waves before they reach the surface. The funnel then has a “closing disk” of some sort, which turbulence necessarily crosses in violation of the assumptions of the quadrupole-less FWH approach. Possible options in this thorny issue include simply omitting the disk from the integral, and including it as if all the assumptions were satisfied. Although neither one is accurate enough in general, it was shown¹⁾ that, with a thorough treatment of the FWH formula and a proper choice of variables, closing the FWH surfaces at the outflow end results in a better prediction of both noise spectra and overall sound intensity.

A typical grid and FWH surface used in the simulations^{1,2)} are shown in Fig.1. Along with the jet plume area, the computational domain contains the outer region around the nozzle wall, which is necessary for a correct prediction of sound propagating upstream. The full LES domain is much larger than the FWH domain. For jets in still air, the FWH domain typically extends to 25-30 D_{jet} streamwise, and the full domain including the buffer layer is 50-60 D_{jet} . This provides damping of the fluctuations in this area and weakens wave reflections at the boundaries. In the

simulations of jets in co-flow, due to the much slower decay of the turbulence, the computational domain is extended in the streamwise direction up to about 80 D_{jet} , with the FWH surfaces as long as 50 D_{jet} . The grid has two overlapping blocks (additional artificial blocks are introduced for parallel computations). This topology seems close to optimal for 3D computations of round and near-round jets. Namely, the inner, Cartesian block is helpful in avoiding a singularity at the axis of the cylindrical coordinates and the outer,

O-type block allows a good control of the grid density and, in particular, a fine distribution where the thin shear layer is located. Fully Cartesian or fully cylindrical topologies seem much less efficient. Note that the computational domain shown in Fig.1 does not include the interior of the nozzle. This was the way the simulations in^{1,2)} were performed: the jet conditions were prescribed as inflow boundary conditions at the nozzle exit.

The numerical system briefly presented above has been applied to a wide range of round jets. These studies showed that it provides a realistic description of the shear-layer roll-up and three-dimensionalization, even in jets with co-flow with velocity up to 60% of the jet’s. This turns out possible thanks to a global instability sustained by the jet-flow when a velocity profile with a thin boundary layer is prescribed at the nozzle exit, and with the high-order numerics used. Other effects that have been predicted with good reliability include: Mach number variation for isothermal jets; cross-effect between the acoustic Mach number and jet heating; effect of co-flow on both isothermal and hot jets; effect of shock-cell/turbulence interaction in a sonic slightly under-expanded (fully expanded Mach number $M_{FE}=1.37$) jet. These simulations, although performed with relatively small grid counts (on the order of one million nodes) resulted in fairly good agreement with experimental data on mean flow and turbulence statistics (when available) and in noise predictions close to the target accuracy of 2-3 dB both in overall directivity and spectra up to $St \approx 1.5$. In addition to jets from round nozzles, “synthetic chevrons” (emulated by altering the inflow conditions) were considered and found to reduce low-frequency noise while increasing mid-frequency noise.

The blemish of the simulations^{1,2)} is that, for subsonic jets, the calculated noise peaks at angles relative to the jet axis around 10° smaller than those in the experiments. Besides, the peak levels are in many cases under-estimated. Other than that, for the under-expanded sonic jet, too smooth a transition to turbulence caused by too dissipative numerics leads to some contamination of the sound spectra.

Nevertheless, in general, the findings of these studies are encouraging, support the credibility of the approach, and justify its application to more complex jet flows, thus progressing in the direction of airliner engines.

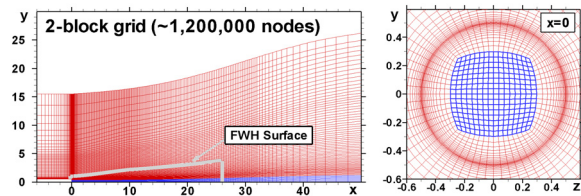


Figure 1. Typical grid: side view through axis and end view at nozzle exit (lengths normalized with D_{jet}).

III. Further Steps Forward

A. Methodological Improvements

1. Local automatic flux-limiters for jets with shocks.

Shock cells, which are often present in airplanes' exhaust jets in cruise flight, are of great importance in the airliner industry. The shocks, naturally, raise the level of numerical difficulty. The demands of shock capturing and those of LES resolution with acceptable numerical dissipation conflict. Probably for this reason, no examples of LES of jets with shock-cells are found in the literature. The approach to shock capturing in LES developed and tested in Refs. 1, 2 turned out to be rather efficient and permitted to reconcile to some extent these contradictory demands. Recall that this approach employs a *zonal* activation (in a-priori prescribed area where strong shocks are expected) of the Van Albada¹⁵⁾ flux-limiter and switching from the 5th to 3rd order scheme in the upwind part of the hybrid (centered/upwind-biased) numerics used in the NTS code everywhere else. This effectively suppressed the instability of the hybrid low-dissipative scheme caused by the interaction of shocks with turbulence for the sonic slightly under-expanded jet of Tanna¹⁶⁾ considered in Ref.2. At the same time, based on the “numerical Schlierens” and density fields from the simulation, there were no spurious oscillations, the shocks were not smeared, and the physical instability of neither the shocks nor the shear layer was suppressed. Note that the zone with active limiters cannot include the shear layers (otherwise the transition to turbulence would be suppressed) and so, in order to preserve numerical stability, the weight of the upwind differences in the hybrid scheme had to be sufficiently high in the initial region of the shear layers¹⁾. This however led to insufficient accuracy of representation of transition to turbulence and, as a result, to appearance of false peaks in the noise spectra²⁾. This and, also, the obvious difficulty of applying a zonal method to complex jets with a-priori unclear shock topology, was the motivation to search for another, more robust, technique, as presented now.

Unlike the zonal method of Refs. 1, 2, the new one is based on an algorithm with a local *automatic* activation of the flux-limiters in the spirit of the work of Hill & Pullin¹⁷⁾. The limiters are introduced independently in different spatial directions. As an example, let us consider the direction i in the computational coordinates.

For computing of the inviscid fluxes at the cell face $(i + 1/2)$ the standard NTS' hybrid numerics is replaced with the pure upwind-biased 3rd order differencing and the van Albada flux-limiters are activated if either the inequality

$$\frac{|p_{i+1} - p_i|}{\min\{p_i, p_{i+1}\}} > \varepsilon = O(1) \quad (1)$$

or the two inequalities

$$[(M)_{i+1} - 1] \cdot [(M)_i - 1] < 0 \quad \text{and} \quad V_n (\partial M / \partial n) < 0 \quad (2)$$

are satisfied, where p is the pressure, V_n is the velocity component normal to the face, M is the Mach number, and ε is set equal 0.5 based on preliminary numerical experiments.

In accordance with the inequality (1), the standard numerics is locally replaced by the more dissipative scheme with flux-limiters, provided that the pressure change between the two adjacent control volumes is “too large” while the inequalities (2) activate the alteration of the standard scheme at the normal shocks, independent of their strength. Considering that shocks in turbulent jets are not stationary (but fluctuate), switching to the 3rd order upwinding and turning on the flux-limiters is carried out not only at the cell face $(i + 1/2)$, where the inequalities (1) or (2) are satisfied, but also at two neighboring faces, $(i - 1/2)$ and $(i + 3/2)$. Other than that, in order to accelerate the sub-iterations convergence the flux-limiters are “frozen” after 2 sub-iterations of a time-step.

The algorithm described above has been tested on cold and hot jets from round and beveled conical nozzles (see Sections B.1 and B.4) and turned out to be robust and more accurate than the zonal one.

2. Two-step, RANS-LES, approach

As mentioned in Section II, none of the simulations presented in Refs.1, 2 include the interior of the nozzle. Instead, the jet flow conditions are prescribed as inflow boundary conditions at the nozzle exit, which assumes that the jet has a uniform core and a thin near-wall boundary layer that may be specified more or less arbitrarily. For simple jets from single round nozzles this approach is quite justified. However beyond this, academic, area, i.e., for jets from complex (e.g., beveled or dual, staggered and offset), nozzles it is non-applicable, since a strong non-

uniformity of the static pressure in the nozzle exit plane and a vectoring of the jet plume are typical of such cases, and therefore, no reasonable a-priori boundary conditions at the exit of such nozzles can be formulated. So the only rigorous way of treating such nozzles is full-scale coupled, nozzle-plume, LES or at least, DES. Unfortunately, at practical Reynolds numbers, this is currently non-affordable whether on our small PC clusters, or on mainframe computers. So, in order to make an LES-based jet-noise prediction possible today, some way to resolve this issue has to be found. One such way consists in a two-stage, RANS-LES, simulation strategy developed and tested in Refs. 18, 19 and in this work.

In the first stage, a coupled nozzle-plume axisymmetric or 3D (depending on the geometry) RANS computation is performed. In 3D, this is not very cheap, but still is quite affordable with grids fine enough to resolve all nozzles' boundary layers and, in any case, is incomparably less expensive than a full LES.

Then, in the second stage, LES is carried out for the jet plume only with the inflow conditions at the nozzle exit taken from the RANS solution obtained in the first step. Note that the grid in the radial direction near the nozzle wall edge used in this LES stage may be 20 times coarser than the RANS grid (resolving the viscous sublayer not being necessary), which is precisely what makes the LES possible.

The specific form of the inflow conditions used in the present study depends on whether the inflow is subsonic or supersonic.

For subsonic inflow, we impose (interpolate from the RANS solution to the LES grid) the profiles of stagnation pressure and temperature, p_t and T_t and, also, the profiles of inflow-velocity angles with respect to the y - and z - axes:

$$\tan(\alpha_y) = u_y / u_x, \quad \tan(\alpha_z) = u_z / u_x. \quad (3)$$

As for the boundary condition for the static pressure, just as in all the previous simulations^{1, 2)}, the 1D non-reflecting boundary condition²⁰⁾ is used:

$$\partial p / \partial t - \max\{(c - u_l), 0\} \cdot (\partial p / \partial l) = 0, \quad (4)$$

where $(\partial / \partial l)$ denotes differentiation along the streamwise grid line, u_l is the corresponding velocity component, and c is the local speed of sound.

For supersonic inflow, all the flow parameters are specified from the RANS solution.

As shown in the next Section (B.1, B.3, and B.4) the two-stage approach outlined above turns out to be not only feasible, but capable of predicting the noise of jets from rather complex nozzles with a reasonably high accuracy.

B. Results and Discussion

1. Single round jets with shocks.

Two such jets have been computed, one studied in the experiment of Tanna¹⁶⁾ (fully expanded Mach number M_{FE} and temperature T_{FE} are equal to 1.372 and 1.0 respectively) and another one from the experiments of Viswanathan²¹⁾ ($M_{FE}=1.56$, stagnation temperature $T_t/T_a=3.2$). The former computation, just as in Ref.2, is carried out within the conventional approach (LES of the jet with uniform inflow profiles and thin boundary layers) and the latter - within the two-step approach outlined above. In both cases the weight of the upwind part of the hybrid scheme is as low as 0.25 starting right at the nozzle exit. As for shock capturing, the algorithm with local flux-limiters defined by Eqs. (1), (2) is used. The grids in the simulations are clustered in the shock-cell region and have around 2.2 and 3.6 million nodes for the cold and hot jets respectively. Results of the simulations and their comparison with the experimental data^{16,21)} are presented in Figs. 2-7.

Figure 2 presents snapshots of the magnitudes of the pressure gradient and vorticity and of the "x-limiter markers" showing the field points where the flux-limiters in the x -direction are active (0 – limiters off, 1 - limiters on). One can see that for Tanna's jet with relatively weak under-expansion ($p_j/p_a=1.61$), the limiters are turned on only in a few very restricted regions of the first three shock cells with high pressure gradients and are passive in the turbulent jet region. The limiters in the two other directions in this case are not activated at all. For the more severe case²¹⁾ ($p_j/p_a=2.12$), the flux-limiters in the x -direction turn out to be active in a somewhat wider area, which includes both the strong oblique shocks and the normal shock closing the first shock cell. In the r -direction, just as in Tanna's jet, the limiters are passive, while in the azimuthal direction (not shown), they work only in some points of the shear layer located in the region right downstream of transition to turbulence (this is triggered by the

inequality (1) and is indirect evidence of a somewhat coarse ϕ -grid which has 64 nodes only). Thus, in general, Fig.2 suggests that the limiters virtually do not affect the resolution of turbulence in the simulations.

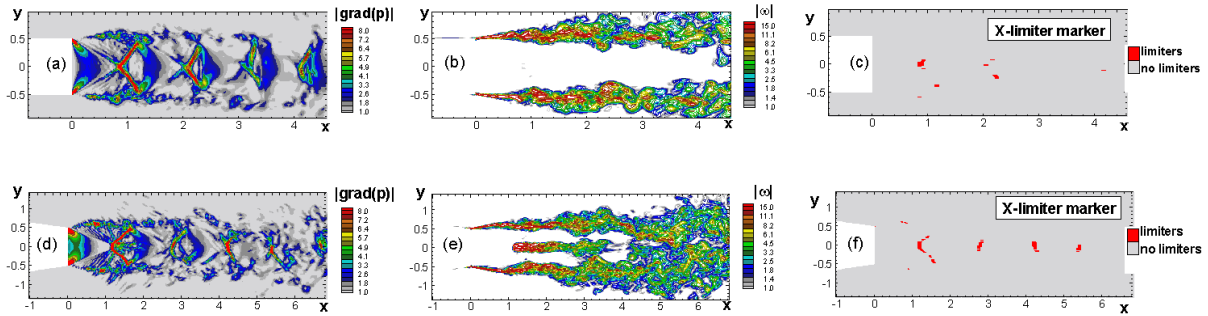


Figure 2. Snapshots of pressure gradient, vorticity, and “x-limiter markers” from simulations of the cold (a-c) and hot (d-f) sonic under-expanded jets.

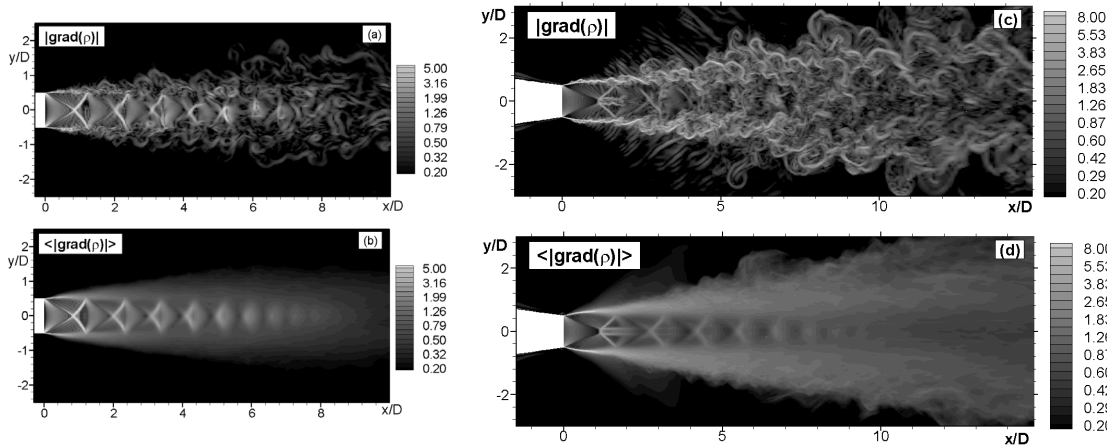


Figure 3. Snapshots (a, c) and time-average (b, d) of magnitude of density gradient (“numerical Schlierens”) for the cold (a, b) and hot (c, d) sonic under-expanded jets.

Figure 3 presents visualizations of both jets in the form of the instantaneous and time-averaged contours of the magnitude of density gradient (“numerical Schlierens”), which visibly illustrate the general flow patterns in both jets and, in particular, display a system of well-resolved shock cells interacting with turbulence. For the strongly under-expanded jet of Ref.21, it also shows the presence of a Mach disc closing the first shock cell and a subsequent subsonic zone and “internal” shear layer which is also clearly seen in the vorticity field in Fig.2e.

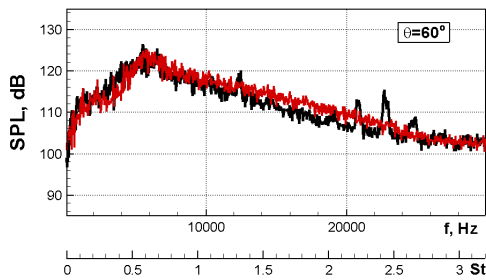


Figure 4. Sound spectra (per unit of Strouhal number) for the cold sonic under-expanded jet obtained with zonal (black) and local (red) limiters. Distance 72 diameters.

Figure 4 compares the performance of the zonal and local automatic (present work) algorithms for shock treatment. It shows that the latter completely eliminates the false peaks in the SPL spectra typical of the zonal algorithm used in Ref.1.

Finally, Figs.5-7 compare the SPL spectra and OASPL directivity curves computed with the use of the local flux-limiters with the corresponding experimental data of Tanna¹⁶) and Viswanathan²¹). As seen in the upper frames of Fig.5, where, along with the SPL spectra computed for the sonic under-expanded jet¹⁶), we present similar spectra for the corresponding (with the same stagnation

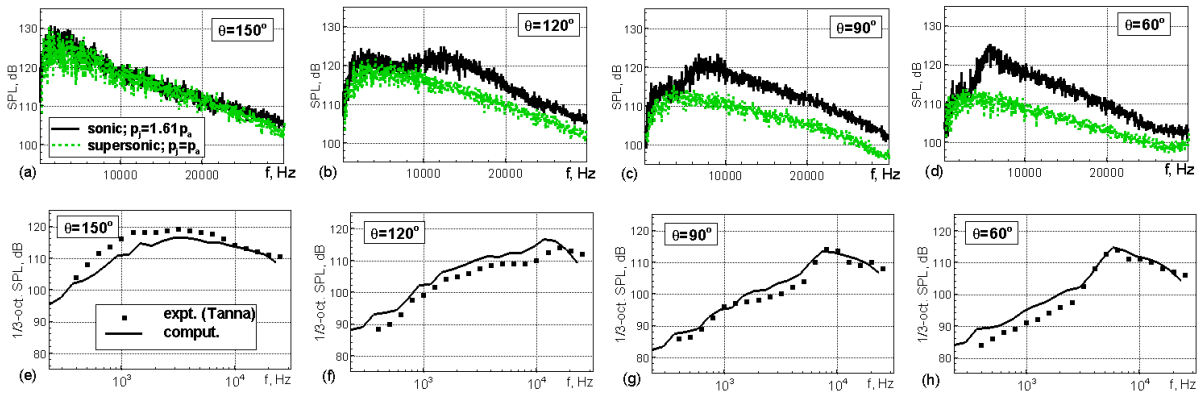


Figure 5. Raw (upper row) and 1/3-octave (lower row) SPL spectra for the cold under-expanded sonic and perfectly expanded supersonic jets at $M_{FE}=1.372$. Experiments from Ref.16. Distance 72 diameters.

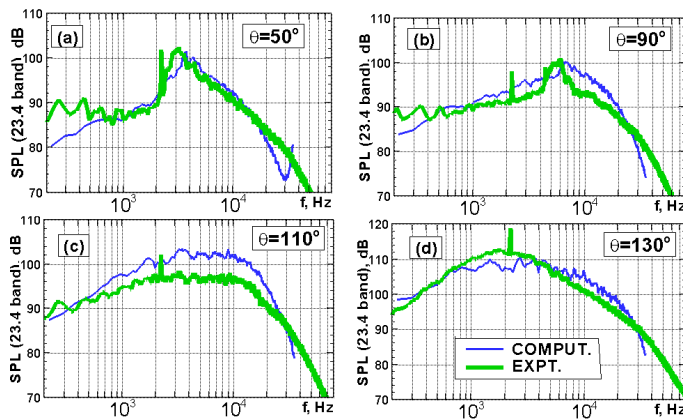


Figure 6. Computed and measured²¹⁾ narrow-band SPL spectra for the hot sonic under-expanded jet at $M_{FE}=1.56$. Distance 98 diameters.

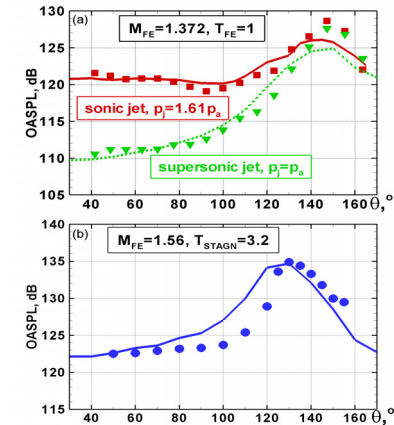


Figure 7. Computed and measured OASPL directivities: (a) – cold jets at $M_{FE}=1.372$ from Ref.16; distance 72 diameters. (b) – hot jet at $M_{FE}=1.56$ from Ref.21; distance 98 diameters.

parameters) supersonic perfectly expanded jet, the simulations correctly represent the broadband shock-cell component of the noise and the shift of its peak towards lower frequencies with decreasing observer angle, θ (the angle is defined with respect to the jet inflow). The lower frames of this figure and Fig.6 show that not only do the simulations capture the spectral shapes for both jets, but they also achieve fairly good quantitative agreement of the noise with the data up to frequencies around 22 kHz ($St \approx 2.5$ and $St \approx 1.8$ for the cold and hot jets respectively). Indirect, but still convincing evidence that the numerics we use correctly represents the shocks and their interaction with turbulence is that at observer angles 50° and 90° (angles at which the broadband shock-cells noise is dominating) the agreement of the predicted spectra with those measured in Ref.21 is very good (see Fig.6a, b). For observer angles 110° and 130° (Fig.6c, d), where the Mach-wave radiation is the dominating noise mechanism, the predicted spectral shapes are also very good, but the “plateau” in the spectrum at 110° is over-predicted by almost 5dB. The OASPL directivity corresponding to the shock-cell noise ($\theta < 90^\circ$) also compares with the data very well (see Fig.7).

Summarizing, we can conclude that algorithm for LES of jets with shocks based on the automatic activation of the flux-limiter presented in Section A.1 above performs quite satisfactorily.

2. Simple co-planar dual jets.

Real turbo-fan engine nozzles are dual, and so the ability to predict the noise of co-annular jets is crucial for any computational tool with a claim to industrial value. Although co-planar nozzles do not introduce any essentially new physics, they demand a significant increase of computing effort compared to single jets. This is caused by the need to resolve two shear layers (this requires increasing the grid count in the radial direction), by the larger radius of the

outer shear layer demanding a refinement of the grid in the azimuthal direction, and by the slower streamwise turbulence decay, especially in co-flow, which demands a longer computational domain and so a larger grid in the streamwise direction. In this section two examples of such flow computations are presented (one in still air and another one in co-flow), both studied in the experiments of GEAE for which results were kindly provided to the authors by Dr. P. Giebe. The simulations are carried out within the “LES of jet only” approach at the following primary and secondary (fan) jet’s parameters: $M_p=0.75$, $M_s=0.85$, $T_p=737^\circ\text{K}$, $T_s=311^\circ\text{K}$, and co-flow Mach number, $M_{CF}=0.28$; the area ratio of the nozzles, $AR=2$ and the diameter ratio, $D_s/D_p=1.77$. The length of the computational domain in the simulations is $75D_p$ for the no co-flow and $120D_p$ for the co-flow cases respectively, with an appropriate elongation (up to $76D_p$) of the FWH surfaces. The grid has ~ 3.2 million nodes total.

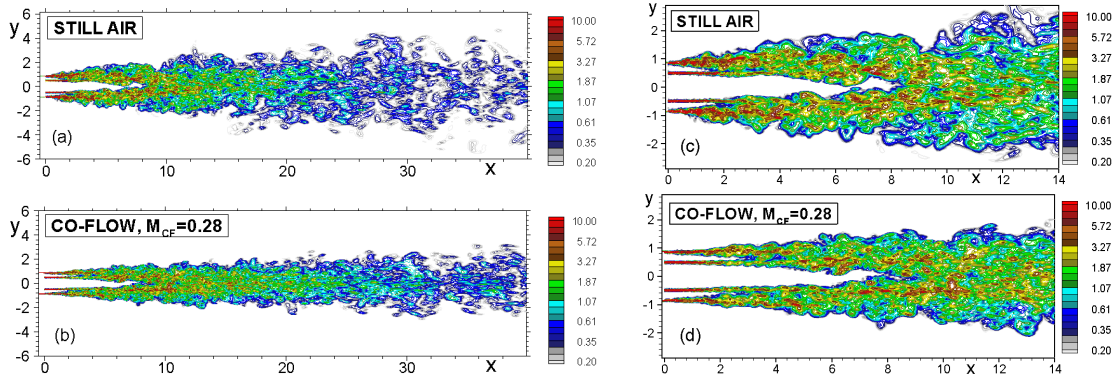


Figure 8. Snapshots of vorticity for coplanar dual jets.

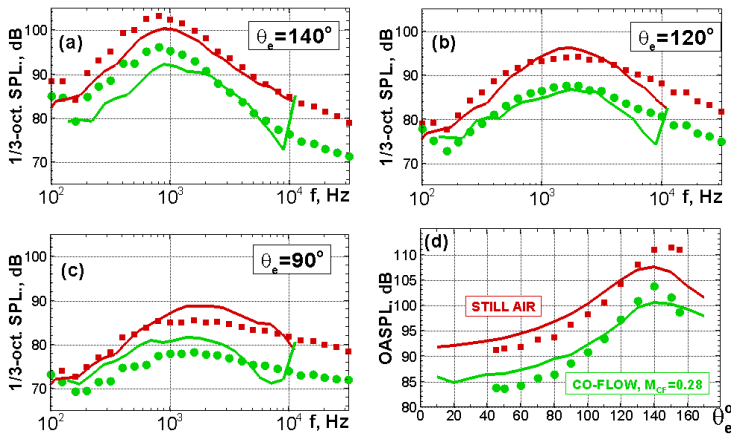


Figure 9. Computed and measured 1/3-octave SPL spectra (a-c) and OASPL directivity (d) for coplanar dual jets in still air (red) and in co-flow (green). Experiments of GEAE. Distance 166 core nozzle diameters.

co-flow on the noise is predicted very accurately. On the other hand, much like for single jets in Ref. 2, the peak noise levels turn out to be underestimated by 2-3dB.

3. Dual jets from staggered nozzle.

The staggering of dual nozzles (see Fig.10) which is typical of real aircraft engines adds new simulation challenges. First of all, in this case the one-stage (LES of jet only) approach is apparently non-applicable (there is no way to prescribe a priori sufficiently-realistic inflow conditions), and so the two-stage, RANS-LES, simulation strategy should be applied. However even this strategy turns out not to be quite sufficient once the real shape of the nozzles is taken into consideration. Indeed, the outer walls of both core and fan nozzles are converging, so that the boundary layers on these walls develop under adverse pressure gradients. The Implicit (with subgrid model off) LES

Figure 8 reveals the drastic effect of co-flow on the jet physics. In particular, it delays transition to turbulence in the outer shear layer (the mechanism of this phenomenon is similar to that discussed for single jets in Ref. 1). As a result, the potential core of the secondary jet becomes longer. This, in turn, leads to a delay of transition of the inner shear layer, which itself is caused by contact with turbulence of the outer shear layer.

Figure 9 demonstrates a fairly good agreement of the noise predictions with experimental data on both spectral and overall sound characteristics up to a frequency of 8 kHz ($St \approx 1.5$ based on the core jet parameters). Note that the effect of the

or ILES we use for jet-flow simulation cannot represent such boundary layers accurately. This would result in their separation accompanied by vortex shedding and, therefore, in a completely wrong solution, in general, and noise prediction, in particular. Ideally, in order to resolve this issue, some hybrid RANS-LES approach or an LES with wall modeling should be used. However, for realistic Re numbers, this would demand a huge grid, unaffordable not only today but also in the near future. So some work-around of this issue should be found. As of today, we use for this purpose the following approximate approach, which can be considered as a simplified zonal RANS-LES.

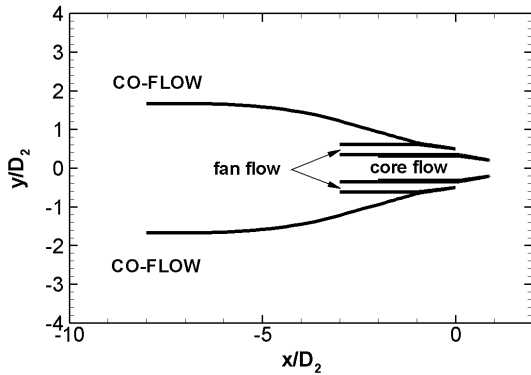


Figure 10. Geometry of dual staggered nozzles studied in experiments of Ref.22.

In the near-wall regions, which include the whole or at least a major part of the boundary layers but do not touch the shear layers, we specify the eddy-viscosity field from the RANS solution obtained in the first stage of the 2-stage RANS-LES approach, and solve the momentum and energy RANS equations with this eddy viscosity field. Solving also the turbulence transport equations in these areas, which would be consistent with a full zonal RANS-LES approach, would demand an r -grid there at least as fine as that used in RANS, i.e., an order of magnitude finer than what is used in the LES stage (a fragment of typical grid with about 4 million nodes total used in this stage for the geometry shown in Fig.10 is presented in Fig.11). In the rest of the computational domain, ILES is used, i.e., ν_t is set to zero with the switch from the RANS ν_t being performed smoothly in a small, geometrically specified, region.

Although no direct quantitative assessment of the accuracy of this approach can be done, as shown below, it turns out to be feasible, succeeds in keeping the boundary layers attached, and permits the prediction of noise with a reasonable accuracy.

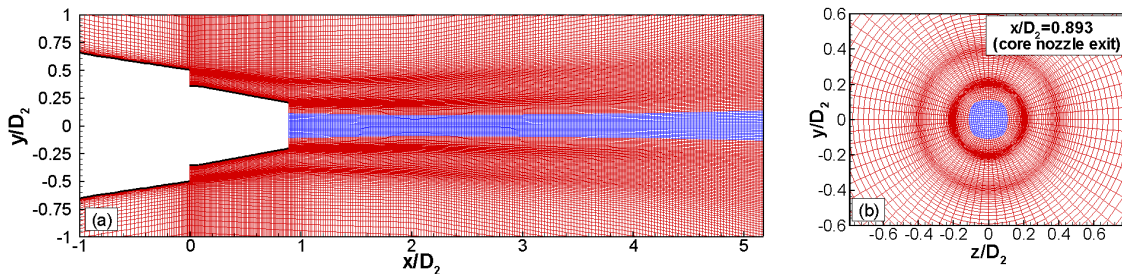


Figure 11. Fragments of grid used in LES of dual jets from staggered nozzles.

The two specific flows considered are the round co-annular jets from the dual staggered nozzle in still air and in co-flowing flow studied in the experiments of Viswanathan²²⁾ at the following conditions: the stagnation nozzle pressure ratio of the primary and secondary jets $NPR_p = NPR_s = 1.8$ and the stagnation-temperature ratios, $(T_t)_p / T_a$ and $(T_t)_s / T_a$, are 2.37 and 1.0 respectively. For the case with co-flow, $M_{CF} = 0.2$. The area ratio of the fan and core nozzles is $AR = 3.0$, the diameter ratio $D_s / D_p = 2.5$, and the bypass ratio, BPR , defined from the RANS computation in the first stage is equal 4.7.

Some results of the computations are presented in Figs. 12-15.

Figure 12 illustrates the pattern of the simulation approach used in the area between the fan and core nozzles. It shows near-nozzle fragments of the ν_t -field from the RANS solution obtained in the first stage of the computation; the part of it used in the second (hybrid RANS-ILES) stage; and finally a vorticity-magnitude snapshot from the latter in the vicinity of the nozzles exit for the case of the jet with co-flow. The figure suggests that no boundary-layer separation is observed upstream of the nozzle exits, and that the non-zero eddy viscosity regions do not overlap with either outer or inner shear layer, which would corrupt the prediction of the transition to turbulence. Thus, as already mentioned, the approach is feasible, although, of course, far from exact, and any error it introduces should be evaluated in the future, when at least a full zonal RANS-LES of the flow becomes possible.

Figure 13 shows instantaneous fields of vorticity magnitude from the simulations of the jets in still air and in co-flow. They visibly display not only the well-known effects of co-flow (narrowing of the jet and elongation of its potential core), which are observed also in simulations of the co-planar dual jets with no account of the real shape of the nozzle (see Fig.8), but also a striking feature that is specific to this real design: the co-flow virtually does not cause a delay of transition in the outer shear layer; such a delay is very pronounced in the co-planar dual jets in co-flow. This is explained by the fact that due to the rather thick turbulent boundary layer forming on the outer wall of the fan nozzle in this laboratory model, the effective co-flow velocity at the outer boundary of the shear layer near the fan-nozzle exit is rather low. One more specific feature of the staggered geometry versus the co-planar one is a very fast transition to turbulence in the inner shear layer. This occurs because the outer shear layer at the location of the core nozzle exit-plane is already turbulent, and so the inner shear layer is subjected to strong external disturbances.

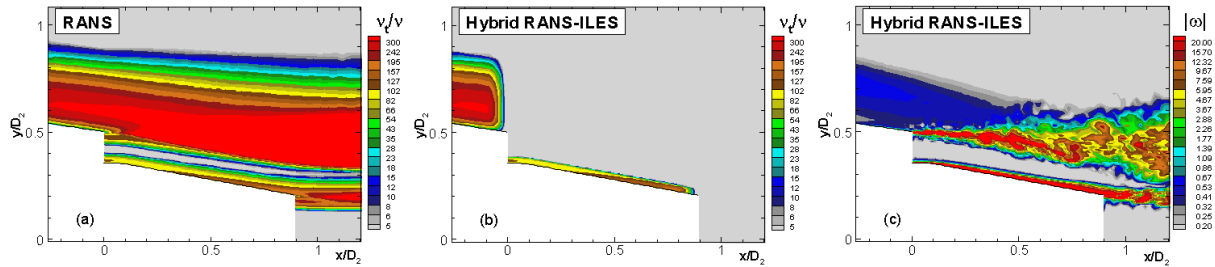


Figure 12. Eddy viscosity field from RANS (a), its part used in zonal RANS-ILES (b), and snapshot of vorticity (c) in the vicinity of fan and core nozzles exit.

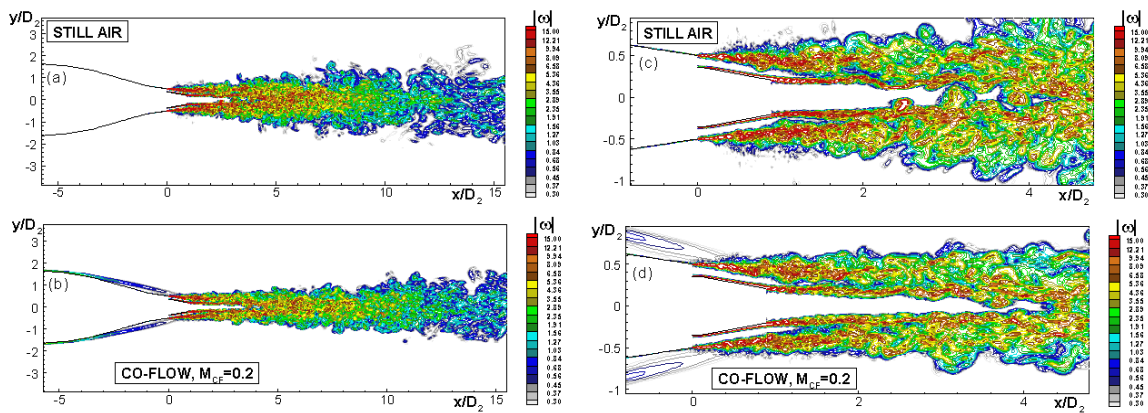


Figure 13. Snapshots of vorticity for dual jets from staggered nozzles.

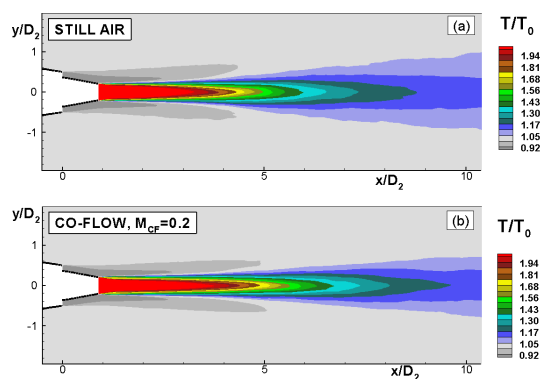


Figure 14. Mean temperature in meridian plane of dual jets from staggered nozzles.

Figure 14 contains time-averaged temperature fields from the two simulations. They are well in line with the vorticity snapshots shown in Fig.13 and, in particular, show the narrowing of the jet in co-flow and elongation of both its primary and secondary potential cores.

Finally, Fig.15 presents results of the noise computation and their comparison with experiment. At $\theta > 120^\circ$ the predicted spectra and OASPL agree with experiment fairly well, although the effect of co-flow is somewhat underestimated. In the lateral direction (θ around 90°) the noise level is quite a bit overestimated, especially for the case with co-flow (the discrepancy in the OASPL reaches 4-5dB). This is most probably caused by the coarseness of the ϕ -grid in the current simulations.

Although the number of the ϕ -nodes is now 72, which is the same as in the grid used for the coplanar jet considered in the previous section, in this case, due to a large diameter of the fan nozzle, the azimuthal grid step $r\Delta\phi$ in the outer shear layer is 1.5 times larger. The coarseness of the grid is also the reason for the false peaks in the high-frequency part of the narrow-band spectra at the frequency around 15 kHz, which corresponds to a Strouhal number around 1.9 based on the core jet parameters.

4. Evaluation of noise-reduction concepts.

As already mentioned in Introduction, as of today, this is a primary practical application of LES. In this section we consider three noise reduction concepts, namely, two relatively recent ones suggested by Viswanathan^{21,23} (beveled nozzles) and by Papamoschou²⁴ (fan-flow deflecting vanes), and the well-known chevron nozzles concept.

4.1. Beveled nozzles. The motivation to this study is multi-fold. First of all, according to the experiments of Viswanathan^{21,23}, who has suggested this design, the beveled nozzles cause a noticeable jet noise reduction. Also, regardless of the industrial value of the design, the unique jet-noise data accumulated in the experiments^{21,23} present in-itself a very attractive database for validation of different CFD/CAA approaches. Additionally, CFD/CAA may be helpful in supporting the experiments, in terms of elucidating physical mechanisms responsible for the noise-reduction provided by the beveled nozzles and probably even an optimization of the nozzle designs.

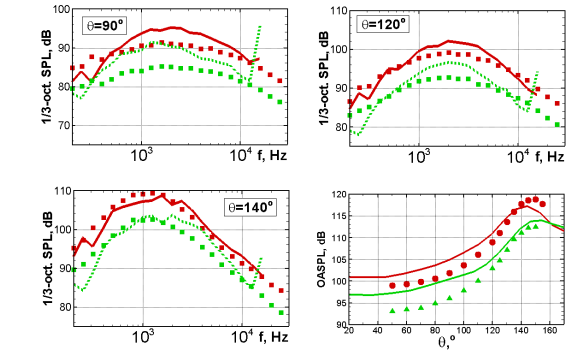
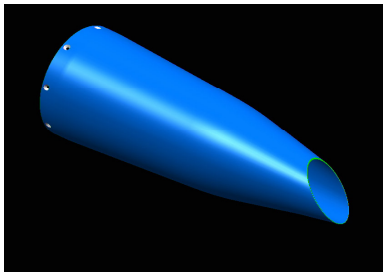


Figure 15. Computed and measured²² 1/3-octave SPL spectra (a-c) and OASPL directivity (d) for dual jets from staggered nozzles, in still air (red) and in co-flow (green). Distance 98 core nozzle diameters.

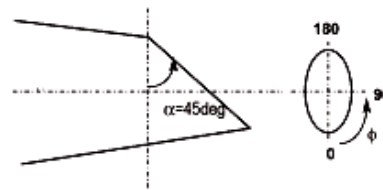


Figure 16. General view of beveled nozzle²¹ and convention on counting of bevel (α) and azimuthal (ϕ) angles.

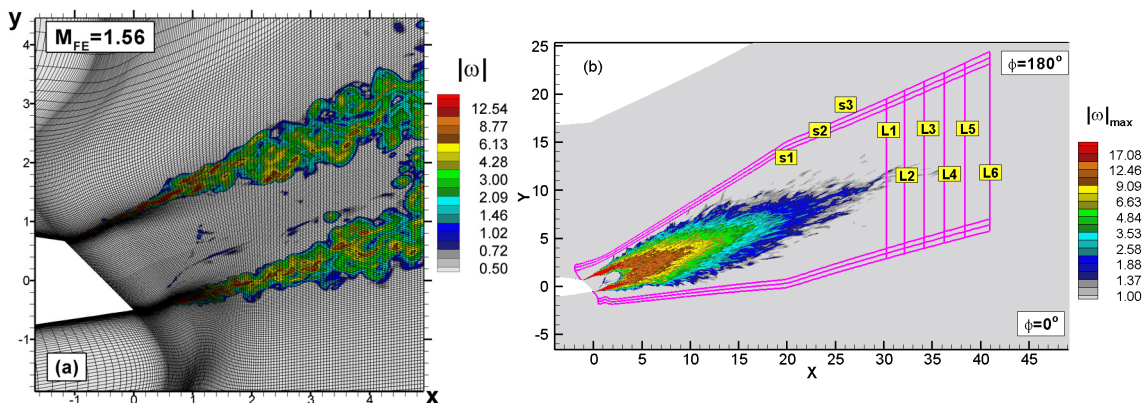


Figure 17. Fragment of LES-grid and snapshot of vorticity near exit of beveled nozzle (a), and a set of nested FWH surfaces in XY-plane together with maximum (over time-sample) vorticity field (b).

In terms of CFD, the design is challenging, first of all, because due to the strong non-uniformity of the static pressure in the nozzle exit plane and plume vectoring, even the single beveled nozzle flows considered in the present work should be computed with the use of the two-stage RANS-LES technology. In this section this technology is applied to the hot ($T_t/T_a=3.2$) jets from the baseline round and beveled nozzles with bevel angle of 45° (see Fig. 16) at 3 different values of the nozzle pressure ratio studied in the experiments²¹): $NPR=1.28$ ($M_{FE}=0.6$), $NPR=1.89$ ($M_{FE}=1$ – sonic perfectly expanded jets), and $NPR=4.0$ ($M_{FE}=1.56$ – sonic strongly under-expanded jet). This series provides for both validation of the numerical system being used and valuable information on the effect of nozzle beveling on the aerodynamic and noise characteristics of the jet at different Mach numbers.

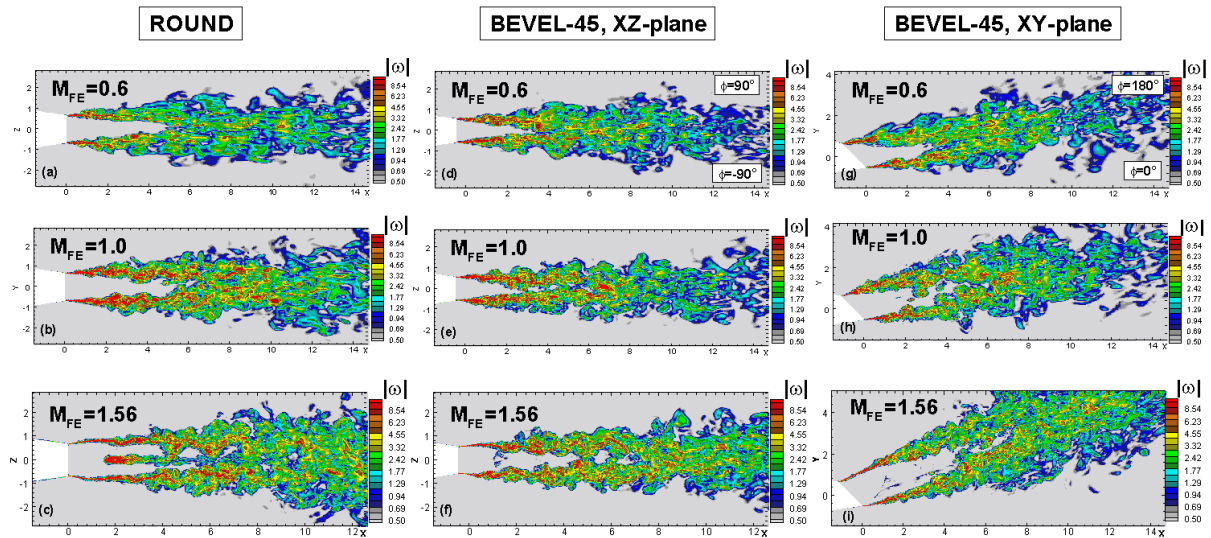


Figure 18. Snapshots of vorticity for round and beveled jets.

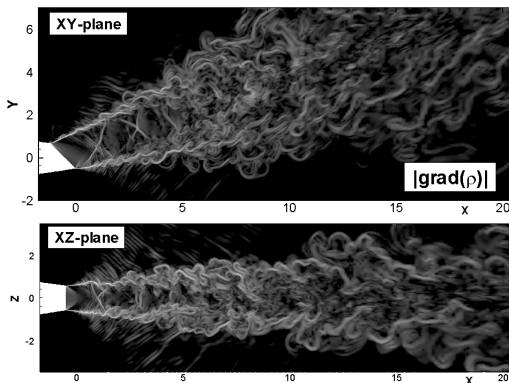


Figure 19. “Numerical Schlierens” for beveled jet at $M_{FE}=1.56$.

detail) are shown in Fig. 17. Note that both the grid and the FWH surfaces (more detail) are adjusted to the plume vectoring. This helps to reduce the total number of nodes in the simulations, which varied from around 1.5 up to 3.6 million nodes. Figure 18 illustrates the effects of nozzle beveling and Mach number on the turbulence structure and general flow pattern. For the turbulence, the only qualitative difference between the round and beveled jets is the “internal” vortical layer forming in the center of the supersonic jet from the round nozzle and associated with formation of the normal shock and “internal” shear layer in this jet mentioned already in Section B.1. In the beveled jet the normal shock does not form. For the general flow pattern, the figure displays a strong non-linear growth of the beveled plume deflection angle in the direction of the shorter nozzle lip (azimuthal angle $\phi=180^\circ$) with Mach-number increase. At the subsonic Mach numbers, the predicted deflection angles are around 9° at $M=0.6$ and 10.5° at

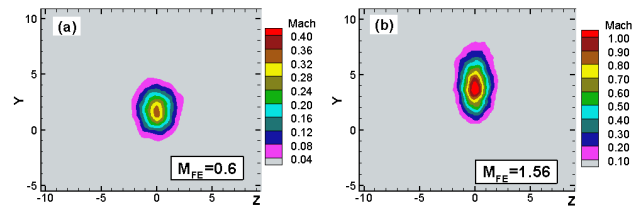


Figure 20. Mean Mach number contours in $x/D=10$ cross-section of beveled jets at different Mach numbers.

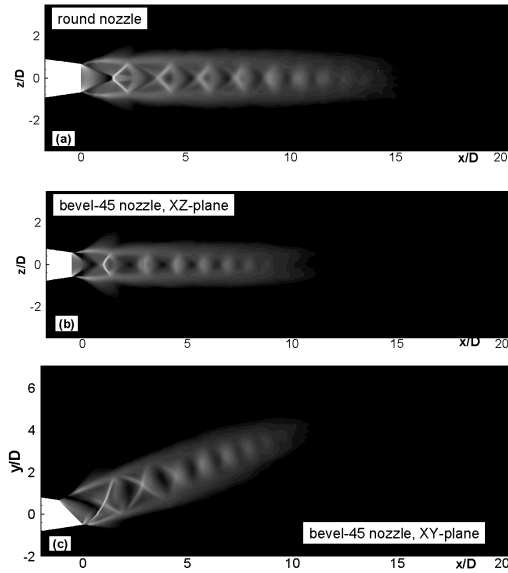


Figure 21. Time-average of magnitude of pressure gradient for round (a) and beveled (b, c) jets at $M_{FE}=1.56$.

$M=1.0$, which agrees fairly well with the experimental value of around 10 degrees²¹⁾. At $M_{FE}=1.56$ the angle reaches nearly 19°, also consistent with experiment. Note, also, that for all the three Mach numbers the nozzle discharge coefficients for the beveled nozzle computed in the first, RANS, stage of the simulations are in a quite good agreement with the data²¹⁾: the measured discharge coefficient is ~13% less compared to the round nozzle, while in the computations the difference is 13.6% for $M_{FE}=1.0$ and 1.56, and 14.5% for $M_{FE}=0.6$. Other than that, Fig.18 suggests that the nozzle beveling causes narrowing of the jet in the plane normal to the symmetry plane XY and slanted to track the jet*, while in the symmetry plane the jet is widening, the effect getting more pronounced when M_{FE} increases.

“Numerical Schlierens” of the under-expanded beveled jet in the XY - and XZ -planes presented in Fig.19 give a more detailed idea of the different wave patterns in the two planes and, just as Fig.18, show that the width of the jet in these planes is rather different.

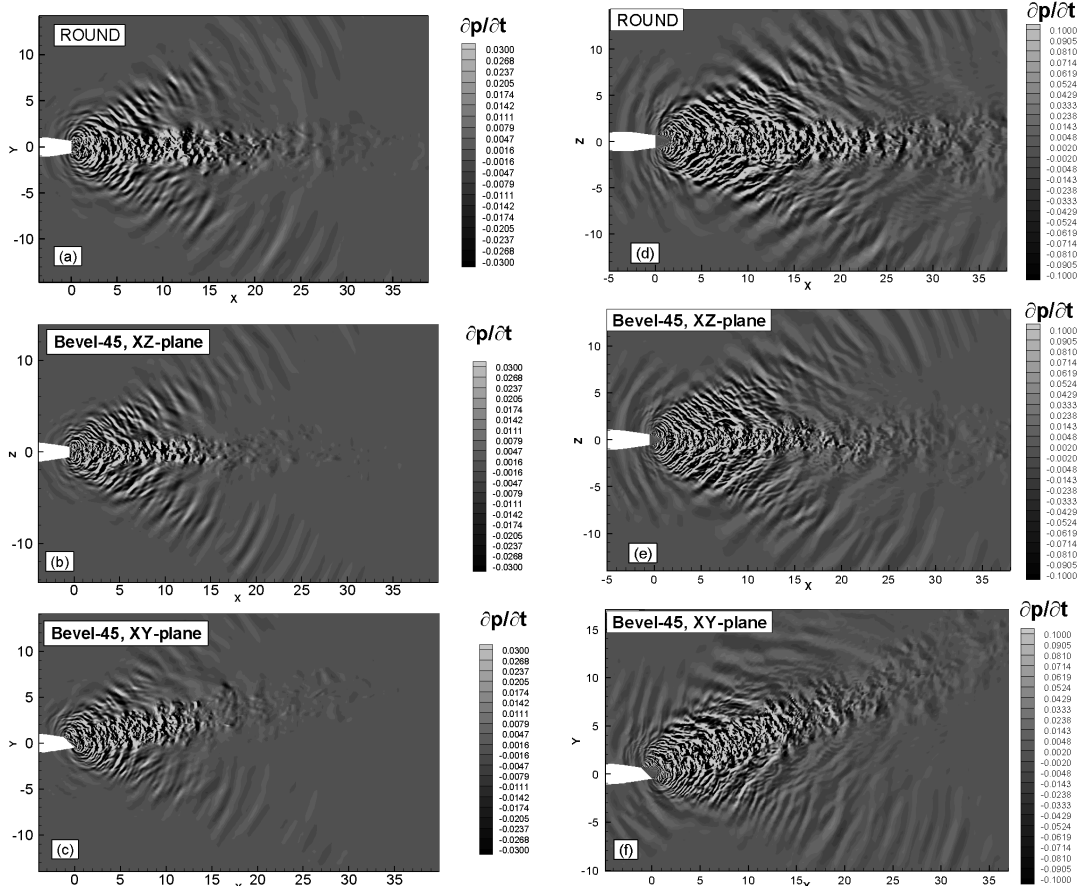


Figure 22. Snapshots of pressure time-derivative (in the acoustic range) for round and beveled jets at $M_{FE}=1.0$ (a-c) and $M_{FE}=1.56$ (d-f). $\partial p / \partial t$ is normalized with ρ_a , c_a , and D .

* In Fig.18 and hereafter, projection of this plane onto the Cartesian XZ -plane is referred to as “ XZ -plane”.

This is explained by the deformation of the jet cross-section (which becomes oval) increasing with growth of the nozzle bevel angle and the jet velocity. The latter trend is demonstrated by Fig.20a, b, where the time-averaged Mach number fields in the section $x=10D$ are plotted for the jets with $M_{FE}=1.56$ and 0.6.

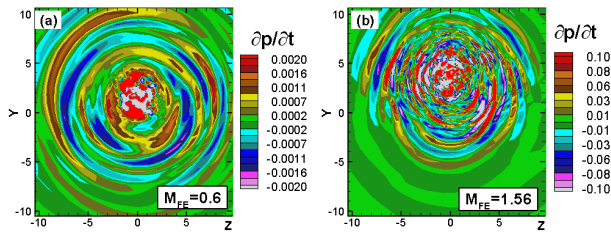


Figure 23. Snapshots of pressure time-derivative in $x/D=10$ cross-section of beveled jets at different Mach numbers.

presented in Fig.22. This figure visually reflects the alteration of the direction of the radiated sound waves in accordance with the plume deflection caused by the beveled nozzle. As far as the effect of M_{FE} is concerned, its increase from 1.0 up to 1.56 results in stronger and shorter sound waves and, also, in a qualitative alteration of the sound waves structure associated with the appearance of broadband shock-cell noise and Mach-wave radiation typical of the high-velocity supersonic under-expanded jets.

Finally, Fig. 23 illustrates the azimuthal non-uniformity of the sound generated by the beveled jets, the effect being rather pronounced at $M_{FE}=1.56$ and virtually negligible at $M_{FE}=0.6$.

One more peculiarity of the supersonic jet from the beveled nozzle, which is clearly seen from a comparison of the time-averaged fields of the magnitude of the pressure gradient in the round and beveled jets at $M_{FE}=1.56$ presented in Fig.21, is a faster damping of the shocks in the beveled jet.

Not surprisingly, the above specific features of the jets from beveled nozzles result in a significant alteration of the noise generated by such jets. This is seen already in the instantaneous XY - and XZ -cuts of the pressure time derivative in the acoustic range for two of the considered Mach numbers

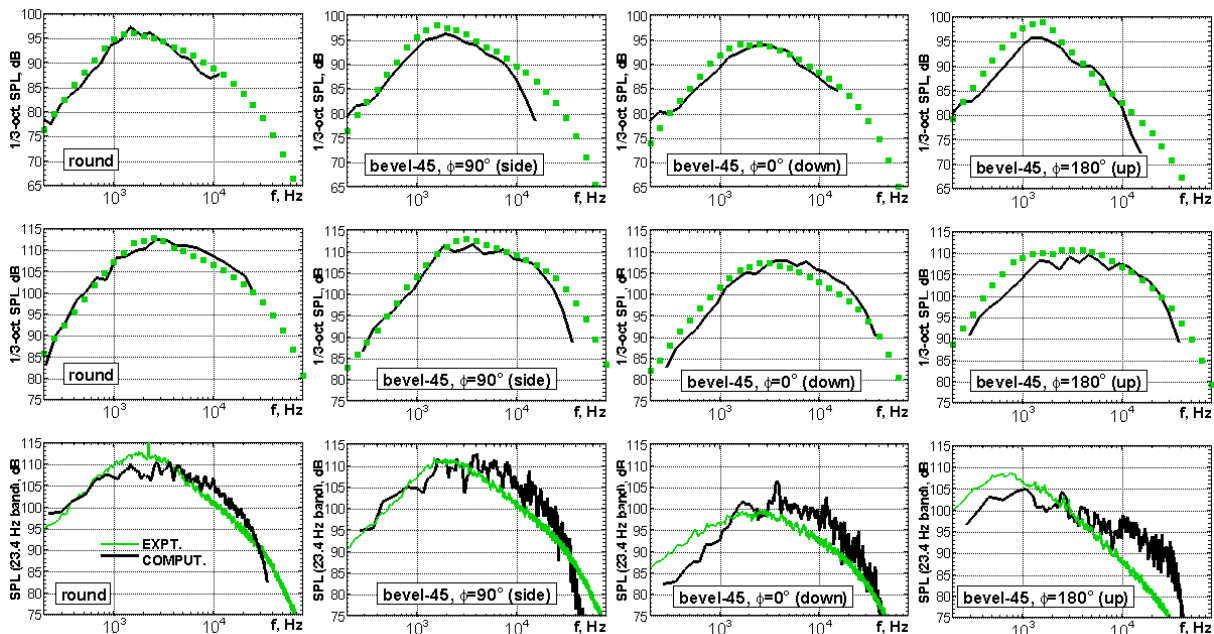


Figure 24. Computed and measured²¹⁾ 1/3-octave (upper and middle rows) and narrow-band (lower row) SPL spectra at $\theta=130^\circ$ for round and beveled jets at $M_{FE}=0.6$ (upper row), $M_{FE}=1.0$ (middle row), and $M_{FE}=1.56$ (lower row). Distance 98 round nozzle diameters.

A quantitative comparison of the noise predictions with the data²¹⁾ is presented in Figs.24, 25 where computed and experimental spectra (1/3-octave for the subsonic jets and narrow-band (23.4 Hz) for the supersonic jets) at $\theta=130^\circ$ and OASPL directivity curves are plotted for all the considered cases.

As far as the spectra are concerned (see Fig.24), in general, the simulations reproduce the spectral shapes fairly well and capture all the trends observed in the experiments. For the round jets, the maximum discrepancy between the predicted and experimental spectra is within 2-3 dB everywhere, except for the directions close to the jets axis

(not shown), where it reaches 4 dB near the spectral maximum. For the beveled jets, the spectral shapes are predicted very well for all the three Mach numbers and all azimuthal directions, and the difference of the predicted and measured spectra is close to that for the round jets, except for the upward ($\phi=180^\circ$) noise from the supersonic jet. In this case the simulation overpredicts the spectral maximum in the lateral direction ($70^\circ < \theta < 100^\circ$) by 5-6 dB.

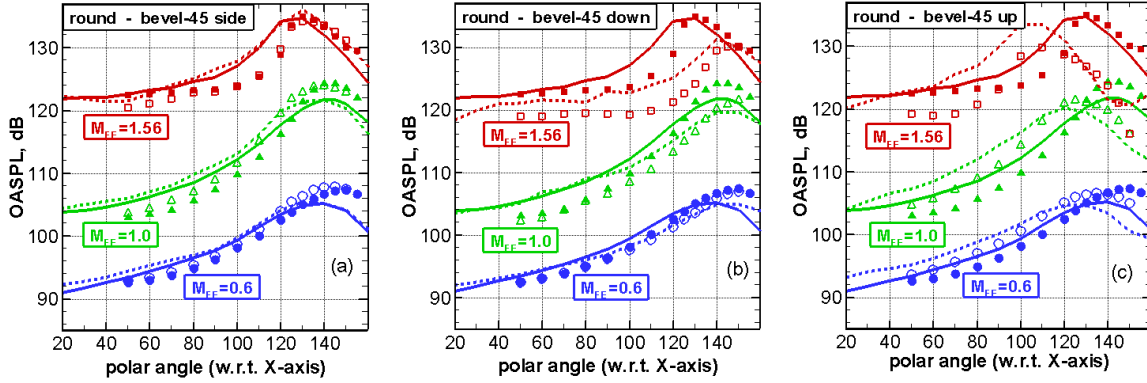


Figure 25. Computed and measured²¹⁾ OASPL polar directivities for round (solid lines for computations, filled symbols for experiment) and beveled (dashed lines and open symbols) jets. Distance 98 round nozzle diameters.

The computed directivity curves (see Fig.25) also reproduce all the trends observed in the experiment. In particular, in both experiments and simulations, the side noise of the beveled jet is virtually the same as that of the round one, while the downward and upward noise reduction caused by the beveled nozzle significantly depends on the Mach number (growing as M increases) and reaches ~ 3.5 dB for the downward noise at $M = 1.56$.

4.2. Dual nozzles with fan-flow deflecting vanes. This design (see Fig.26) suggested by Papamoschou²⁴⁾ is shown to provide a significant (up to 5-7 dB in some experiments) peak-noise reduction in the downward direction. On the other hand, at all azimuthal angles, the noise in the lateral direction (θ around 90°) increases, and it seems that the success of the concept will hinge on the balance between the benefit at some angles and the penalty at others; chevrons raise similar issues. Considering this, CFD/CAA evaluation of this technology could not only provide its deeper understanding, but also suggest ways of optimizing it.

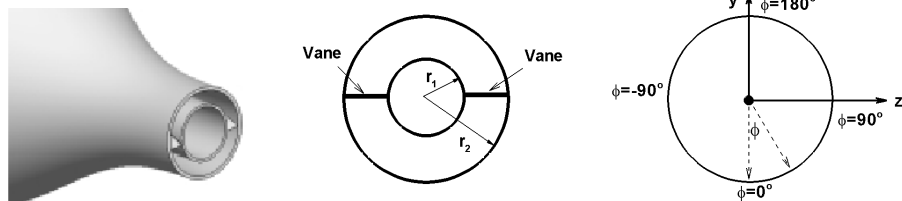


Figure 26. General view of the dual coplanar nozzles with fan-deflecting vanes²⁴⁾ and convention on counting of azimuthal angle ϕ .

In principle, the simulation of this flow should be carried out with the use of the two-stage, RANS-LES, procedure presented in section A.2. However, this would require gridding of the design for RANS computations, which does not seem to be justified at this preliminary stage of the study. Instead, we preferred to “mimic” the effect of the vanes on the velocity field at the nozzle exit with the use of the following formulas for the components of the velocity vector \mathbf{V}^{vanes} induced by the vanes:

$$u_\phi^{vanes} = -V_{max} \frac{u_x^{base}}{U_{fan}^{base}} \frac{r_p}{r} \sin^n \phi, \quad u_x^{vanes} = -2.5V_{max} \cos \phi \sin^n \phi, \quad (5)$$

where u_ϕ^{vanes} and u_x^{vanes} are the azimuthal and streamwise components of \mathbf{V}^{vanes} , V_{\max} is the parameter controlling the maximum value of the azimuthal velocity u_ϕ^{vanes} , u_x^{base} and U_{fan}^{base} are the local and core values of the streamwise velocity component in the fan nozzle exit plane for the baseline (without vanes) nozzle, r_p is the radius of the primary nozzle, and $r_p < r < r_s$ is the radial coordinate (r_s is the radius of the secondary (fan) nozzle). The parameter n is an odd integer, which controls the compactness of the velocity disturbance defined by (5); it is adjusted to reflect the number of vanes, or their position upstream of the nozzle exit.

Relations (5) approximately emulate vanes installed at $\phi = \pm 90^\circ$ or in pairs symmetric with respect to that direction, and provide an irrotational velocity field. If we assume that the streamwise velocity at the exit of the baseline nozzle is uniform, i.e., that $u_x^{base} = U_{fan}^{base}$, then the plume deflection angle provided by the vanes emulated by (5) can be evaluated as:

$$\tan \varepsilon = \frac{\bar{u}_y^{vanes}}{U_{fan}^{base}} = c_n \frac{V_{\max}}{U_{fan}^{base}} \frac{r_p}{r_p + r_s} \quad (6)$$

where \bar{u}_y^{vanes} is the average vertical velocity and $c_n = (2/\pi) \int_0^\pi (\sin \phi)^{n+1} d\phi$.

Accounting for of the vane-induced velocities, the inflow velocity angles α_y and α_z defined by Eqs. (3) in section A.2 can be computed as:

$$\tan(\alpha_y) = \frac{u_y^{base} + u_y^{vanes}}{u_x^{base} + u_x^{vanes}}, \quad \tan(\alpha_z) = \frac{u_z^{base} + u_z^{vanes}}{u_x^{base} + u_x^{vanes}}, \quad (7)$$

where u_x^{vanes} , u_y^{vanes} , u_z^{vanes} are the Cartesian components of the velocity vector \mathbf{V}^{vanes} computed by (5).

The emulation procedure was applied to the dual co-planar jet described in section B.2 above. In particular, the simulations of this jet both in still air and in co-flow presented there were repeated with the vane emulation at $n=3$ (“diffuse vanes impact”) and 7 (“compact vanes impact”). The parameter V_{\max} in (5) was adjusted to set the value of the deflection angle defined by Eq. (6) to 4° (this value is recommended in Ref.24 as close to optimal) at both $n=3$ and 7. Note that no experimental data on the effect of vanes on the jets in co-flow are available in the literature. So its numerical evaluation is very important, since the concept seems to be based on “angling” the fan shear layer away from the core flow, which may strongly interact with co-flow.

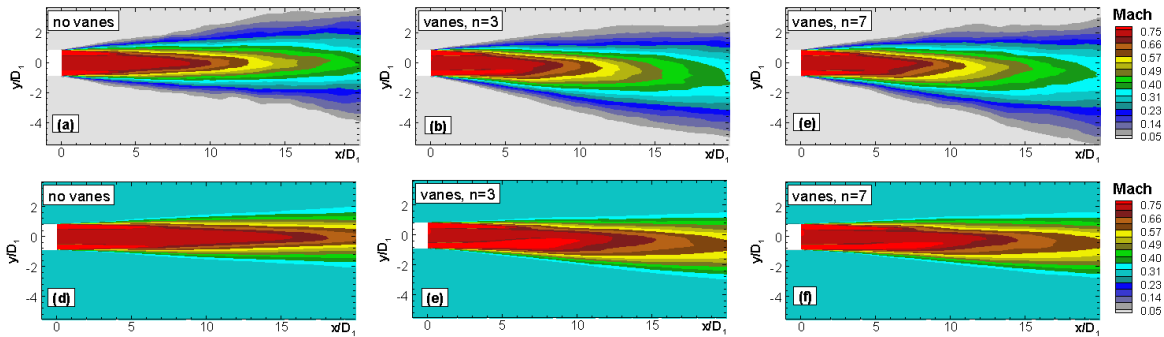


Figure 27. Effect of vanes and “vanes impact compactness” parameter n on mean Mach number fields in symmetry-plane of dual jets in still air (upper row) and in co-flow (lower row).

Figure 27 illustrates the effect of the vanes at the two values of n on the mean flow Mach number in the symmetry plane XY . This effect is quite visual and, based on what is known from experiments for the jet in still air²⁴⁾, seems to be qualitatively correct. Namely, the vanes cause a shortening of the upper and an elongation of the

lower potential cores of the fan flow, and narrowing and thickening of the corresponding shear layers. Also, the Mach-number and velocity fields (not shown) reveal a “fold” in the lower shear layer also observed in experiments. For the cases with co-flow, all these trends are the same and are even more pronounced, in spite of the lower deflection angle (about 1° versus 3° for the jet in still air). As far as the influence of the compactness (the value of n) is concerned, it is non-significant, although at $n=3$ the effect of vanes is somewhat stronger than at $n=7$.

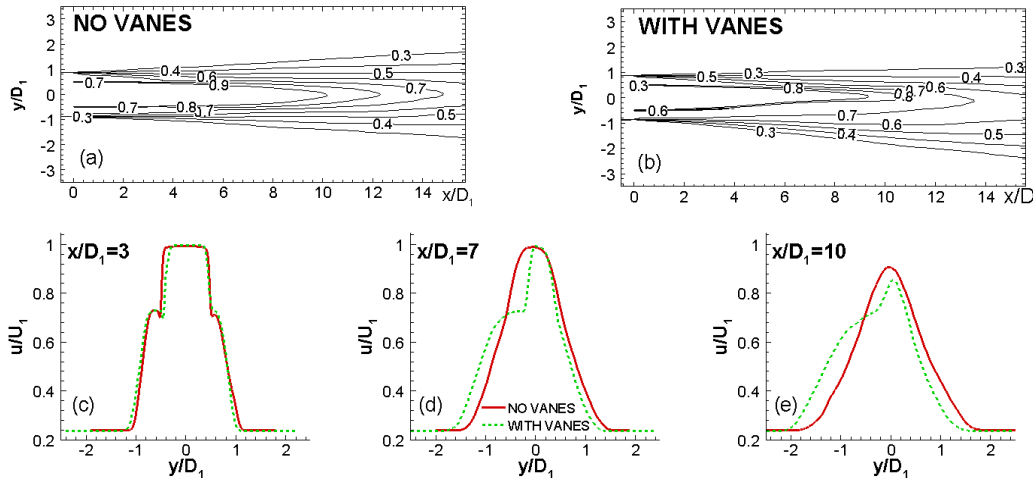


Figure 28. Effect of vanes on mean streamwise velocity contours (a, b) and profiles (c-e) in symmetry-plane of dual jets in co-flow ($n=3$).

Quantitatively, the effect of the vanes on the mean flow at $n=3$ for the jet in co-flow is shown in Fig.28, where we present corresponding streamwise-velocity contours in the XY -plane of the jet and velocity profiles in different cross-sections. In particular, the crease in the shear layer is clearly seen in the velocity profiles, which reveal a strong asymmetry of the jet. Also, the profiles in the lower shear layer have three inflexion points up to $x/D_p = 10$ at least. In other words, the “generalized potential core”²⁴⁾ in this part of the fan flow is somewhat longer than the potential core of the primary flow (the latter is about $\sim 9 D_p$ if defined by $u_{\max}/U_p = 0.9$). The length of the generalized potential core in the upper part of the fan flow is about $5 D_p$, i.e., it is shorter than the secondary potential core of the baseline flow (about $6 D_p$). All these trends are also observed in the experiments and in our simulations (not shown) of the jet in still air.

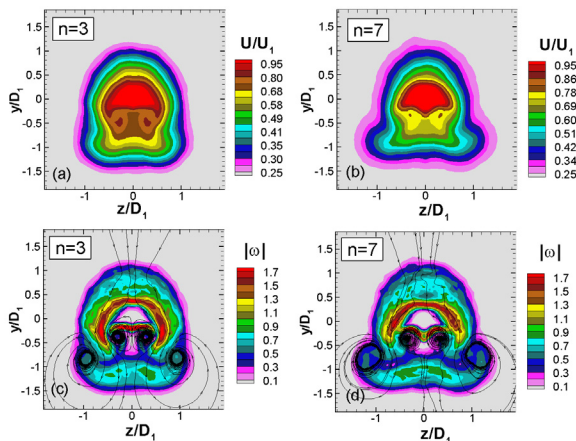


Figure 29. Effect of “vanes impact compactness” parameter n on mean velocity (a, b) and vorticity (c, d) fields in $x/D_p=6$ cross-section of dual jets with fan-deflecting vanes in co-flow.

Figure 29 illustrates the effect of the vanes on the cross-section of the jet in co-flow. It shows, in particular, that the side-deformation of the jet cross-section turns out to be somewhat stronger at $n=7$ (compact vanes impact). The figures suggest that the deformation is caused by two pairs of streamwise vortices created by the vanes (they are seen in Fig.29c, d, where the “in plane” streamlines are plotted together with the contours of the vorticity magnitude).

Finally, Figs.30, 31 display the effect of the vanes on the noise generated by the jet. Figure 30 compares the OASPL polar directivities of the round jets with the corresponding jets with vanes, at different azimuthal angles. It shows that in all the cases the vanes result in a noticeable reduction of the downward OASPL in the vicinity of the peak radiation direction ($\theta=140^\circ-150^\circ$) and in some “penalty” (increase of the noise) for polar angles

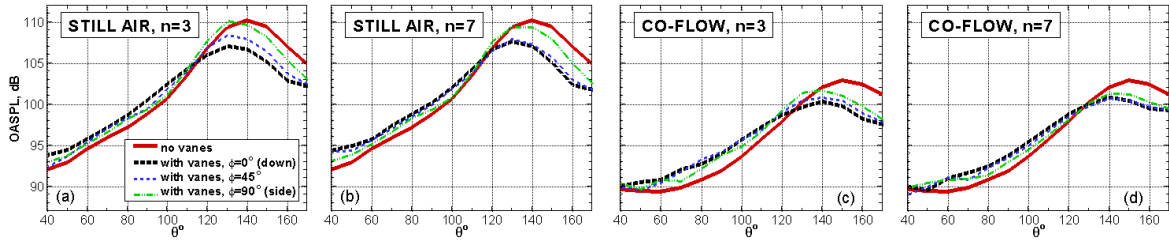


Figure 30. Effect of vanes on OASPL polar directivity of dual jets. Distance 166 core nozzle diameters.

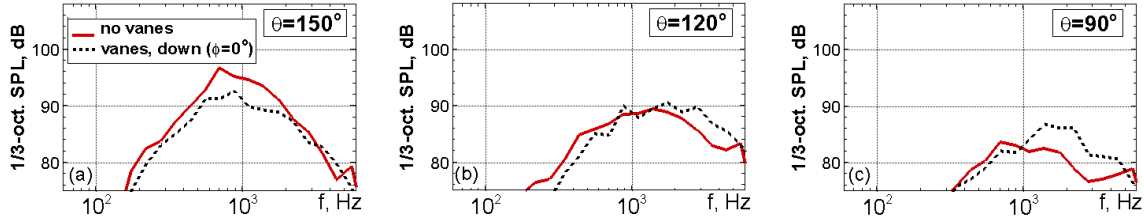


Figure 31. Effect of vanes on 1/3-octave spectra in the downward direction for dual jets in co-flow ($n=3$).

$\theta < 110^\circ$, which comes from the high frequencies (see typical 1/3 octave spectra in Fig.31); this is reminiscent of chevrons, and both devices inject streamwise vortices, which stretch the shear layer. For the jet in still air the noise reduction is 4-5dB, and the penalty is around 1dB, while in co-flow these numbers are 2-4dB and ~ 2 dB respectively. These figures must be taken in the context of the frequency limitation of LES, as usual. So the efficiency of vanes in co-flow seems to be somewhat lower than in still air. On the other hand, the noise reduction caused by the vanes in co-flow is more uniform in the azimuthal direction. Considering that the level of the sideline noise is also important for airplane certification, this cannot be ignored. The effect of the parameter n (vanes impact compactness), in general, is not significant, although at $n=3$ the azimuthal variation of the noise is somewhat stronger than at $n=7$, which is consistent with the difference in the jet cross-section deformation discussed above.

In general, the results show that the fan-flow deflecting vanes are competitive with other known noise-reduction concepts, e.g., with chevron nozzles. However, it should be kept in mind that the vanes may be difficult to implement in a real engine, where the fan nozzle needs to slide back to uncover the thrust reverses. This means that the vanes cannot be anchored to the fan nozzle. So from this standpoint, the designs with non-axisymmetric nozzles (e.g., those with mild offsetting of the fan nozzle, or with mildly beveled core nozzle), which, similar to the vanes, produce a jet deflection, may be preferable. That could be done smoothly and may result in not less or even more pronounced noise-reduction effect. On the other hand, the vanes would be much easier to rotate for different effects at take-off and in cruise, for instance.

4.3. Jets from chevron nozzles. This noise-reduction concept is currently the most popular, and relatively well studied experimentally at great cost. Nonetheless, apart from the “gross” effect of chevrons (decreasing the low- and increasing the high-frequency noise), the detail knowledge about this concept still remains rather restricted, and does not permit the design of an optimal system. Thus a reliable prediction of the noise of jets from chevron nozzles, with a full description of the turbulence field, is an important practical problem. Experimental measurements remain very slow, and of questionable accuracy at least in some regions for this purpose. The approach to this problem used here is similar to that presented in the previous section for the dual nozzles with fan-flow deflecting vanes, i.e., it is based on chevron emulation. This is justified by the difficulty of applying in this case the full-scale two-stage procedure (see section A.2), due to the more complex shape of the exit of chevron nozzles.

An emulation procedure based on an appropriate modification of the inflow conditions by the addition of a set of sources and sinks with zero net mass flow and number equal to the number of chevrons, N_{chev} , was proposed in Ref.2. In that first application, the source/sink parameters were adjusted manually to approximately reproduce the shape of the shear layer. In the present work, this procedure is extended in order to link its parameters with the concrete characteristics of chevrons (their length and angle) directly, and to make it possible to account for the actual (e.g., conical) shape of the chevron nozzles in the framework of the emulation.

The modified emulation procedure is as follows.

The sources and sinks are positioned at a distance X_{SRC} upstream of the nozzle exit, and at a distance R_{SRC} from the nozzle axis. The polar angles of the sources (ϕ_{kR}, ϕ_{kL}) and the sinks ($\tilde{\phi}_{kR}, \tilde{\phi}_{kL}$) are defined as:

$$\phi_{kR} = \phi_k + A_\phi \frac{\Delta\phi_{chev}}{4}, \quad \phi_{kL} = \phi_k - A_\phi \frac{\Delta\phi_{chev}}{4}, \quad \phi_k = k\Delta\phi_{chev}, \quad (8a)$$

$$\tilde{\phi}_{kR} = \tilde{\phi}_k + A_\phi \frac{\Delta\phi_{chev}}{4}, \quad \tilde{\phi}_{kL} = \tilde{\phi}_k - A_\phi \frac{\Delta\phi_{chev}}{4}, \quad \tilde{\phi}_k = (k-1/2)\Delta\phi_{chev} \quad (8b)$$

where $k = 1, 2, \dots, N_{chev}$ and $\Delta\phi_{chev} = 2\pi / N_{chev}$.

Then the velocity-vector, \mathbf{V}^{chev} , induced by chevrons at the point \mathbf{r} of the nozzle exit plane is given by

$$\frac{\mathbf{V}^{chev}}{u_x^{base}} = \frac{1}{2} A_s P_{chev} \Delta r_0 \sum_{k=1}^{N_{chev}} \left[\frac{\mathbf{r} - \mathbf{r}_{kL}^+}{|\mathbf{r} - \mathbf{r}_{kL}^+|^3} + \frac{\mathbf{r} - \mathbf{r}_{kR}^+}{|\mathbf{r} - \mathbf{r}_{kR}^+|^3} - \frac{\mathbf{r} - \mathbf{r}_{kL}^-}{|\mathbf{r} - \mathbf{r}_{kL}^-|^3} - \frac{\mathbf{r} - \mathbf{r}_{kR}^-}{|\mathbf{r} - \mathbf{r}_{kR}^-|^3} \right], \quad (9)$$

where $P_{chev} = L_{chev} \tan(\alpha_{chev})$ is the chevron ‘‘penetration’’ parameter, L_{chev} is the length of chevrons, α_{chev} is the angle between chevron and the nozzle axis. The parameter Δr_0 is the distance from the source/sink located at $\mathbf{r}_{kR}^\pm, \mathbf{r}_{kL}^\pm$ to the edge of a round baseline nozzle used for chevrons emulation. It is assumed to be proportional to the length of chevrons $\Delta r_0 = A_r L_{chev}$.

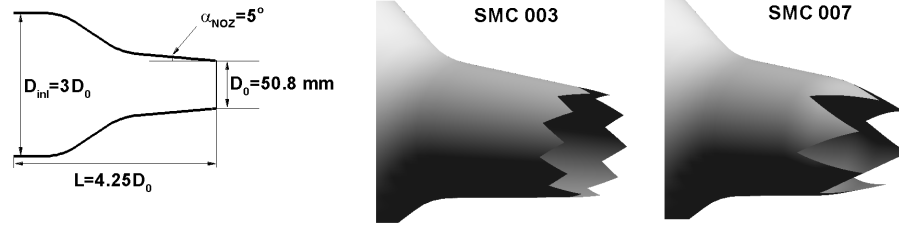


Figure 32. Geometry of round nozzle SMC000 and general view of two chevron nozzles (models SMC003 and SMC007) from Ref.25.

For a choice of the baseline nozzle, it seems natural to choose it as a round nozzle, which has the same flow rate as that of the considered chevron nozzle. Based on the experiments of Bridges and Brown²⁵⁾, who studied a wide variety of chevron nozzles (two of them are shown in Fig.32), this demand is satisfied reasonably well by a nozzle with its exit plane passing through the middle of chevrons. For this nozzle, a coupled (nozzle-plume) RANS computation is carried out which provides the fields of total temperature and pressure and of the background velocity vector \mathbf{V}^{base} . The latter is used to define the inflow velocity angles (3), which enter the inflow boundary condition for the jet-only computations with emulated chevrons, similar to what is done for the nozzle with deflecting vanes (see Eq. (7)).

The emulation formulas (8)-(9) contain four ‘‘free’’ parameters: A_s, A_r, A_ϕ and the angle β_0 between the line connecting a source/sink and the nozzle edge and the x axis. These are non-dimensional and presumed universal. Their values were adjusted based on comparisons between RANS computations with gridded and with emulated chevrons for the nozzles presented in Table 1 for one of the two regimes studied in Ref.25, namely, for the hot, $T_j / T_a = 2.7$, jet with acoustic Mach number 0.9 (jet Mach number 0.55). The range of angles is quite wide, and the planform of the chevrons typical of industrial applications. For this purpose, RANS solutions are sufficient, since the influence of the turbulence treatment is still very weak at the exit plane.

Table 1
Characteristics of chevron nozzles studied in experiments of Bridges and Brown²⁵⁾

Nozzle model	N_{chev}	$\alpha_{chev}, ^\circ$	L_{chev}/D_0	P_{chev}/D_0
SMC000	0	-	-	-
SMC001	6	5	0.45	0.039
SMC002	4	5	0.63	0.055
SMC003	10	5	0.28	0.024
SMC004	5	5	0.52	0.045
SMC006	6	18.2	0.45	0.141
SMC007	6	13.3	0.63	0.145
SMC008	10	13.0	0.38	0.085

Good values for the parameters turned out to be:

$$A_s = 0.42, A_r = 0.12, A_\phi = 0.35, \beta_0 = 35.3^\circ \quad (\sin \beta_0 = 1/\sqrt{3}). \quad (10)$$

In Fig.33, as an illustration of the accuracy of representation of the real chevron nozzles provided by the new emulation procedure with these values of the parameters, we present contours of streamwise velocity at $x/D_0=1.0$, computed with the use of chevron emulation (Eqs.(8)-(10)) and obtained from coupled nozzle-plume RANS solutions with the chevrons gridded, for four of the nozzles from Table 1: SMC001 and SMC007 with 6 chevrons, SMC003 and SMC008 with 10 chevrons with low (SMC001, SMC003) and high (SMC007, SMC008) penetration. The agreement is quite good.

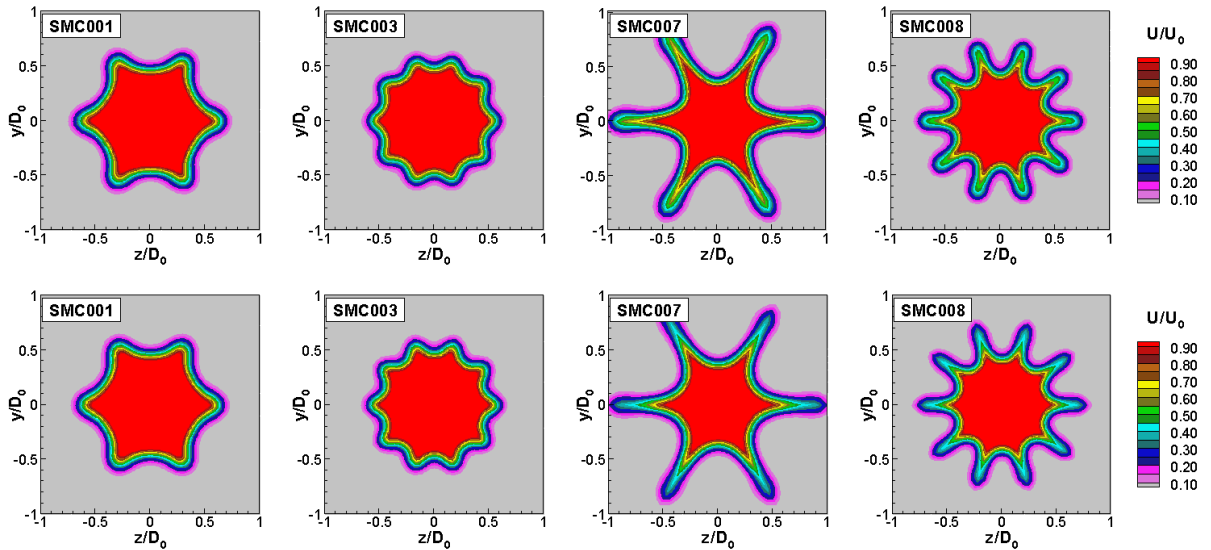


Figure 33. Streamwise velocity contours in $x/D_0=1$ cross-section of jets from different chevron nozzles obtained from RANS with gridding (upper row) and emulation (lower row) of chevrons.

Note that these parameters are not exactly universal in terms of both chevrons geometry and jet parameters, especially NPR . However, they serve as a good starting point for fine-tuning of virtually arbitrary jets in any reasonable chevron nozzle geometry.

LES and noise computations with the use of the chevron emulation procedure outlined above were performed for two of the chevron nozzles considered in Ref.25, namely, for SMC003 and SMC007 (see Fig.32). In addition, a simulation of the baseline round nozzle SMC000 also shown in Fig.32 was carried out as a basis for the evaluation of the effect of chevrons. Note that the nozzles SMC003 and SMC007 present two extremes in the design space studied in Ref.25, and in this sense they are quite representative.

Indeed, according to the experiments, the model SMC003 produces the weakest disturbances and virtually does not affect the jet's aerodynamics. Nonetheless, a small reduction of the low-frequency noise near the peak radiation direction ($\theta=150^\circ$) was observed, with no noticeable high-frequency penalty in OASPL, as is typical of chevron nozzles. Other than that, a marginal shift of the spectra to higher frequencies is registered at θ close to 90° , with no increase of the spectral peaks. Thus, this case permits to find out whether the emulation approach is capable of representing these subtle effects seen in the experiment.

The model SMC007 is an other extreme with a strong effect of chevrons on both aerodynamics and noise. For the aerodynamics, with this nozzle, a significant decrease of the length of the jet potential core and increase of the rate of centerline velocity decay in the initial jet region were observed in the experiment. For the noise, its significant decrease at low frequencies and decrease of the spectral peaks near the peak radiation direction were observed, along with the drop of the maximum of OASPL by $\sim 3.5\text{dB}$ and its shift towards upstream angles (from 150° to $\sim 135^\circ$). Other than that, the high-frequency noise at $\theta < 120^\circ$ increases significantly with a penalty in OASPL of around 1.5dB . Finally, a strong shift of the $1/3$ -octave spectral peaks (from $St \sim 0.5$ for the round jet to $St \sim 2-3$ for SMC007) was observed at $\theta < 100^\circ$. Thus this case is a good test of the approach under extreme conditions.

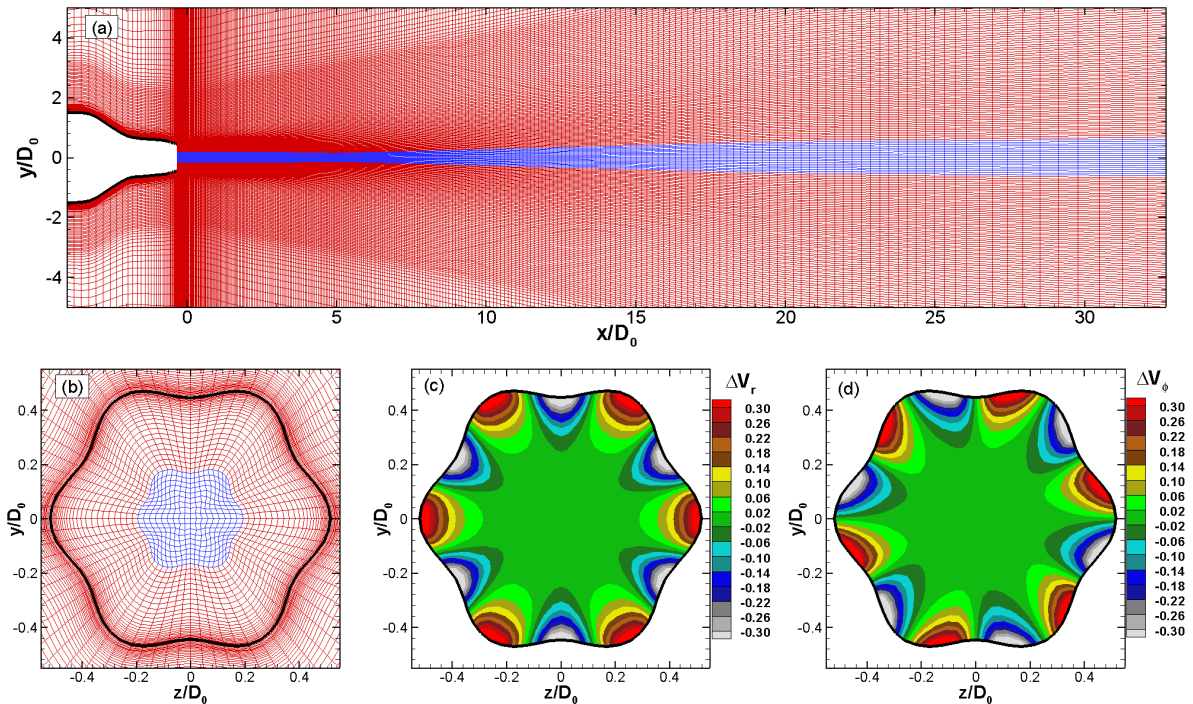


Figure 34. Fragments of grid used in LES of jet from SMC007 nozzle with chevrons emulation (a, b) and “chevron-induced” velocity (Eq. (9)) in nozzle exit plane (c, d).

An example of the grid used in LES of the chevron nozzle SMC007 together with contours of the velocity induced by chevrons in the exit plane of the nozzle is presented in Fig.34. Note that the region with a small r -step in the grid is much wider than in our other simulations. This is needed to provide a better resolution of the vigorously expanding jet boundary. The FWH surfaces are also placed in this region, thus providing for a better resolution of rather high sound frequencies (up to $St \sim 4$ – see below).

Another specific feature of the grid is its modification in the nozzles exit plane needed to ensure a fine resolution of the initial region of the shear layers, as proposed in Ref.2. The modification consists in decreasing the local nozzle radius at the azimuthal angles corresponding to the chevron positions and increasing it between the chevrons, with the amplitude of deformation equal to $P_{chev}/2$; this again amounts to placing the plane half-way between the chevron peaks and valleys. An appropriate smooth deformation of the rest of the grid in the vicinity of the nozzle exit is performed as well. The total number of nodes in the grids used for all the three simulations is around 3 million.

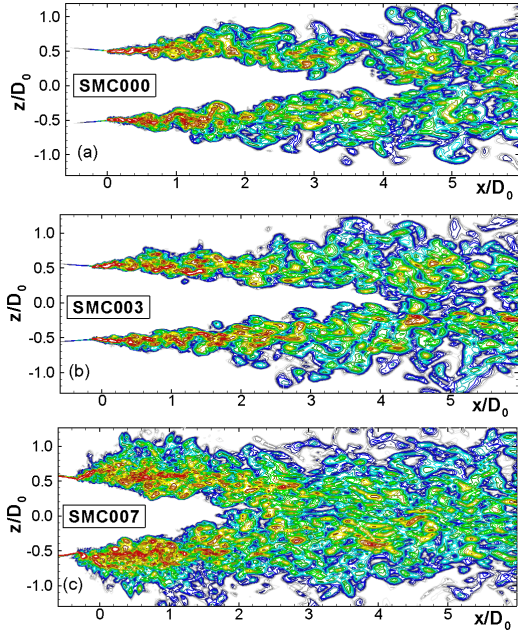


Figure 35. Snapshots of vorticity in XZ -plane of jets from round (a) and chevron (b, c) nozzles.

Results of the simulations are presented in Figs.35-40.

As expected, for the high-penetrating chevrons (SMC007), vorticity snapshots in the XZ -plane shown in Fig. 35 (a plane which passes between the chevrons) reveal a drastic effect of the chevrons on the flowfield, in general, and on the turbulence structure in the shear layers, in particular. Transition to turbulence is very fast, the shear layers are very thick, and the potential core of the jet is much shorter than that of the SMC003 and of the round nozzle (Fig.35a, b); this is often described as “increased mixing.” Other than that, a large number of small vortical structures form both in the shear layer itself and downstream of the end of the potential core of the jet, where almost no large vortices (compared with those forming in the case of the nozzles SMC000 and SMC003) are observed.

Also as expected, the effect of chevrons for the nozzle with “shallow” chevron penetration (SMC003) is marginal, and the corresponding flow pattern is pretty much the same as that for the SMC000 round nozzle, except for a minor deflection of the shear layer from the jet axis in the XZ -plane (Fig.35b) and in the opposite direction in the XY -plane (not shown).

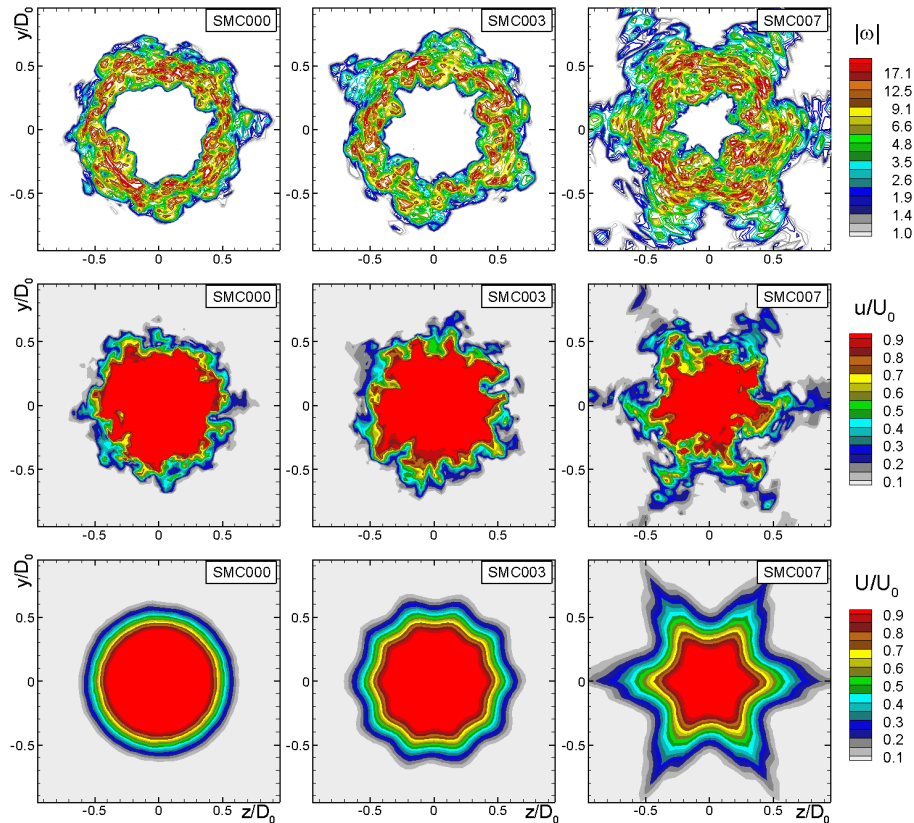


Figure 36. Snapshots of vorticity and velocity (upper and middle rows) and mean velocity contours (lower row) in $x/D_0=1$ cross-section of jets from round and chevron nozzles.

Figure 36 presents typical x -cuts of the instantaneous vorticity magnitude and instantaneous and time-averaged streamwise velocity for the three jets considered. The vorticity snapshots reveal the same features as those discussed above with regard to the meridian cuts in Fig.35, namely, an intensification of the fine-scale turbulent structures and a faster collapse of the jet potential core with deeply penetrating chevrons. Other than that, in spite of the strongly chaotic instantaneous fields, the time-averaged fields are quite regular and reveal the well-known daisy-like shape of the jets; this is a testimony to the sufficient length of the time samples.

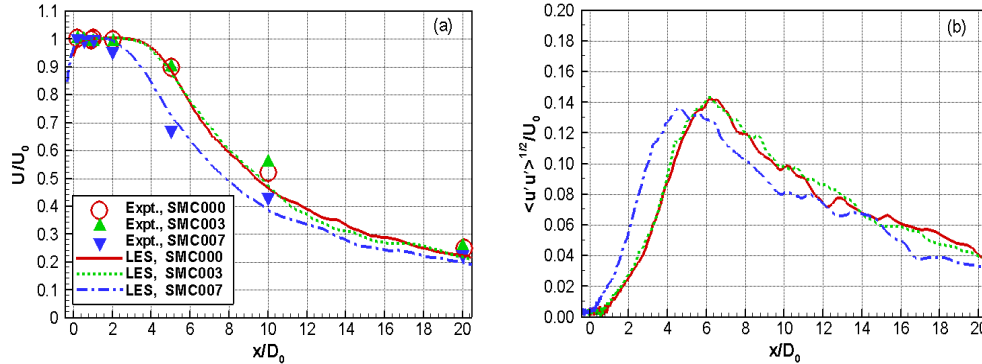


Figure 37. Computed and measured²⁵⁾ streamwise distributions of mean centerline velocity (a) and its root-mean-square fluctuations (b) for jets from round and chevron nozzles.

Unfortunately, a quantitative comparison of the flow patterns from LES of the chevron jets with the experimental surveys presented in Ref.25 is difficult. However, qualitatively, all the trends observed in the experiments are reproduced in the simulations quite correctly. This is supported by a quantitative comparison of the predicted and measured centerline velocity distributions shown in Fig.37. The agreement of the LES with the data is fairly good for both the length of the potential core and the rate of the velocity decay for all three cases. The figure shows, also, that in the simulation, just as in the experiment, the velocity distribution for the chevron nozzle SMC003 is virtually the same as that for the round nozzle SMC000, while for the nozzle SMC007 it is quite different. Note that the same is true for the centerline kinetic turbulence energy distributions from the simulations (these distributions are not available in Ref.25).

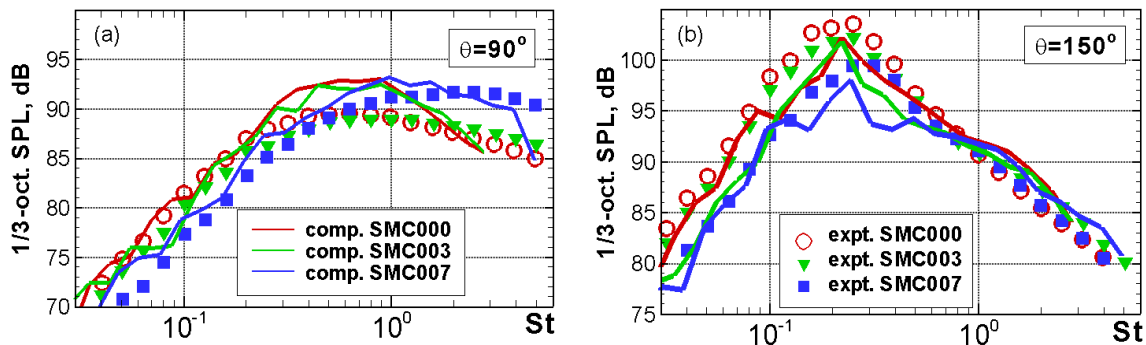


Figure 38. Computed and measured²⁵⁾ 1/3-octave SPL spectra for jets from round and chevron nozzles. Distance 40 effective nozzle diameters.

Figures 38-40 present the 1/3-octave SPL spectra at two observer angles, the SPL maps, and OASPL directivities together with available experimental data. Quite consistently with the effect of the chevrons on the aerodynamic characteristics, the noise generated by the jet from the SMC003 nozzle is very close to that of the jet from the round nozzle SMC000: only a marginal reduction of the low-frequency noise in the peak radiation direction and a weak shift of the spectra to higher frequencies at $\theta = 90^\circ$ are observed. In contrast, for the jet from the SMC007 nozzle, both the reduction of the low-frequency spectral content and OASPL in the peak radiation direction ($\theta = 130^\circ - 150^\circ$) are very pronounced, as is the shift of the maximum of the OASPL curve to less shallow angles.

At observer angles $\theta < 120^\circ$, this jet, on the contrary, generates much louder high-frequency noise than the jets from SMC000 and SMC003 nozzles, and the corresponding spectral peaks are shifted significantly towards higher frequencies (from $St_{\max} \approx 0.5 - 0.6$ for SMC000 and SMC003 to $St_{\max} \approx 1.5$ for SMC007).

As for the agreement of the noise predictions with experiment, in general, it is quite good. Somewhat unexpectedly, the best agreement is reached for the SMC007 nozzle, which has the most complex geometry. The discrepancy between the computed and measured OASPL for this case is about 2.5dB at $\theta = 150^\circ - 160^\circ$ and is much less at all the other angles. The same is true for the spectra up to St number value as high as 4. The higher frequencies are not resolved by the grid used, which is clearly seen in the spectra (steep drop of the blue curves at $St > 4$ in Fig.38) and, also, in the SPL maps (high “density” of the contours near the right boundary in Fig.39f).

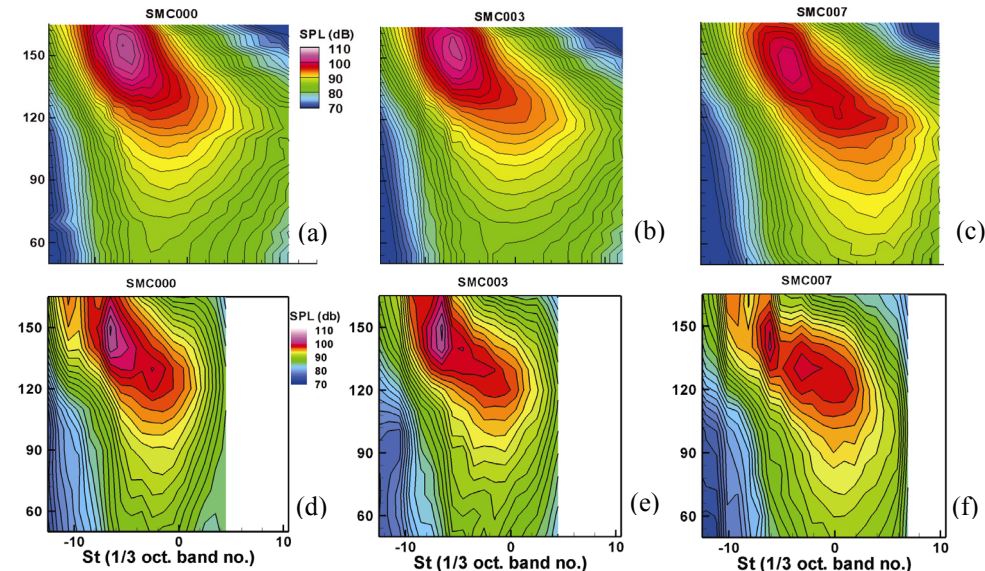


Figure 39. Measured²⁵⁾ (upper row) and computed (lower row) 1/3-octave SPL maps for jets from round and chevron nozzles. Distance 40 effective nozzle diameters. Band number is $10\log_{10}(St)$.

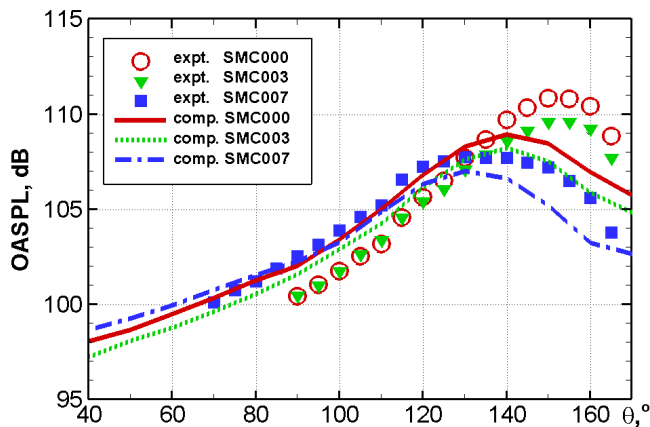


Figure 40. Computed and measured²⁵⁾ OASPL directivities for jets from round and chevron nozzles. Distance 40 effective nozzle diameters.

For the jets from the SMC000 and SMC003 nozzles the agreement with experiment is somewhat worse than for SMC007. In particular, at $\theta = 160^\circ$, the simulation underestimates the OASPL by 3.5dB and over the remaining angles the discrepancy is in the range of 2-3dB. Predicted maxima of the OASPL curves are shifted versus the experimental ones by around 10° (see Fig.40). Other than that, the spectral maxima for these two jets at $\theta = 90^\circ$ are overestimated by around 3dB, and the drop of the spectra after the maxima is faster than in the experiment. Considering that the grids for these jets both in the turbulent region and in the vicinity of the FWH surfaces are no coarser than the grid used for the SMC007 jet, it can be conjectured that the worse prediction of the high-frequency part

of the spectra is caused not by errors in sound propagation, but by the inability of the LES to reproduce the transition process quite correctly and, in particular, to “create” small enough eddies which are responsible for the high-

frequency noise. Thus chevrons with deep penetration help precipitate the transition to turbulence and formation of small eddies; in this sense, simulation of jets from such chevron nozzles is easier than from the round ones and those with less penetrating chevrons.

Finally, all three simulations predict excessively sharp spectral maxima at $\theta = 140^\circ - 150^\circ$ (at $St \approx 0.22$) with some noise “deficit” on both sides of the maximum (see the spectra in Fig.38b and SPL maps in Fig.39). It is precisely this deficit, rather than a minor underestimation of the spectral maxima themselves, which results in the underestimation of the OASPL at these observer angles.

Summarizing, based on the results presented above, it may be concluded that the simulations capture most of the experimentally observed trends in chevron effects, both on jets aerodynamics and noise. Quantitatively, the agreement with the data remains quite acceptable, even though the grids are relatively small. The only two effects the simulations fail to predict are the marginal (1-1.5dB) reduction of the spectral maximum of the noise produced by the jet from SMC003 nozzle at $\theta = 150^\circ$ and some (around 2dB) increase of the spectral maximum at $\theta = 90^\circ$ for the jet from SMC007 nozzle. Note, also, that actually, the agreement of the simulation with the data might be even better, if we were to introduce appropriate corrections accounting for a relatively short arc-distance from the nozzles ($50D$) the noise was measured at in Ref.25. The reason is that at this distance the far-field observer angle and the measurement angle are arguably different, because the true origin of the sound is not at the nozzle exit. Therefore, the experimental directivity curve should be shifted to lower angles. If we consider that the source is located $2D$ downstream of the end of the potential core, then the shift is around 4 degrees at $\theta = 150^\circ$ and 7 degrees at $\theta = 100^\circ$ for SMC000 and SMC003 (the shift is less for SMC007).

IV. Conclusion and Outlook

The development of the LES-based jet-noise prediction technology is proceeding, and several specific improvements are presented here, with most encouraging results. The clearest new capability is that of simulating staggered nozzles, with the core and fan cowls both included, but the chevron and fan-vane emulation procedures have made significant steps, which now quantitatively link the flow fields to the nozzle geometry. The emphasis is on addressing the full complexity of industrial flows, both in terms of geometry and of intense flow effects such as shocks, while checking the accuracy and keeping track of the limitations of LES, especially in terms of frequency, every step of the way. At this stage, the mathematical challenges appear to have been largely mastered, and the CPU power to be the essential obstacle to unrestricted performance. An exception to this is the fact that actual aircraft geometries have additional geometry features (pylon, heat shield, etc.) which will, in the long run, steer CFD towards unstructured grids; however, these have so far hardly been compatible with the high-order, low-dissipation qualities that are clearly needed of the numerics for this kind of simulation. Easy use by non-experts will also not be achieved for quite some time. Another area for sustained attention is the mechanism of transition in the shear layers; all dependence on the grid, numerics, and (for other teams) unsteady forcing will not be eliminated for a long time. Again, CPU-power gains by orders of magnitude would remove the problem, but waiting is not an option.

The most fruitful use of LES today is to produce the turbulent fields that create the noise, thus greatly supporting the experiments which still are the core of noise-reduction technology development, because (given enough care) they cover all frequencies and their reliability is better understood than that of LES (although by no means perfect). This also has to do with the background of the current corps of noise-reduction experts. LES will, at some point, suggest new inventions. For instance, a source of ideas that has not been tapped is the content of the noise in terms of azimuthal wave number m ; if specific m values were found to be most damaging, devices capable of interfering with flow mechanisms at that value should be envisioned. At the simplest level, this would suggest promising values for the number of chevrons. Such information is only a matter of post-processing in LES, but would require massive instrumentation. Similarly, LES is not limited in terms of co-flow (flight) velocity, but most experimental facilities are. Further work will include a search for the cause of the remaining inaccuracies of the predictions the directions near the jet axis. Offset-stream noise-reduction concepts will be pursued, and simulations emulating the straining and offsetting effects of the wing and flaps over the jet will be considered.

Acknowledgments

This work was primarily funded by Boeing Commercial Airplanes and, partially, by General Electric Aircraft Engines, under the supervision of Drs. P. Gliebe and R. Cedar. The authors also thank Dr. K. Viswanathan for providing the experimental data and fruitful discussions and Prof. D. Papamoschou for his helpful comments.

References

- ¹Shur, M.L., Spalart, P.R., Strelets, M.Kh., "Noise Prediction for Increasingly Complex Jets. Part I: Methods and Tests," *International Journal of Aeroacoustics*, Vol. 4, No. 3+4, 2005, pp. 213-246.
- ²Shur, M.L., Spalart, P.R., Strelets, M.Kh., "Noise Prediction for Increasingly Complex Jets. Part II: Applications," *International Journal of Aeroacoustics*, Vol. 4, No. 3+4, 2005, pp. 247-266.
- ³Andersson, N., Eriksson, L.-E., Davidson, L., "Large-Eddy Simulation of Subsonic Turbulent Jets and Their Radiated Sound," *AIAA Journal*, Vol. 43, No. 9, 2005, pp. 1899-1912.
- ⁴Andersson, N., Eriksson, L.-E., Davidson, L., "LES Prediction of Flow and Acoustic Field of a Coaxial Jet," *11th AIAA/CEAS Aeroacoustics Conference, 23-25 May 2005, Monterey, California*, AIAA Paper 2005-2884, 2005.
- ⁵Bodony, D.J., Lele, S.K., "On Using Large-Eddy Simulation for Prediction of Noise from Cold and Heated Turbulent Jets," *Physics of Fluids*, Vol. 17, 085103, 2005.
- ⁶Bodony, D.J., Lele, S.K., "Generation of Low Frequency Sound in Turbulent Jets," *11th AIAA/CEAS Aeroacoustics Conference, 23-25 May 2005, Monterey, California*, AIAA Paper 2005-3041, 2005.
- ⁷Bogey, C., Bailly, C., "Effects of Inflow Conditions and Forcing on Subsonic Jet Flows and Noise," *AIAA Journal*, Vol. 43, No. 5, 2005, pp. 1000-1007.
- ⁸Bogey, C., Bailly, C., "Investigation of Sound Sources in Subsonic Jets Using Causality Methods on LES Data," *11th AIAA/CEAS Aeroacoustics Conference, 23-25 May 2005, Monterey, California*, AIAA Paper 2005-2885, 2005.
- ⁹Lew, P., Blaisdell, G.A., Lyrintzis, A.S., "Recent Progress of Hot Jet Aeroacoustics Using 3-D Large-Eddy Simulation," *11th AIAA/CEAS Aeroacoustics Conference, 23-25 May 2005, Monterey, California*, AIAA Paper 2005-3084, 2005.
- ¹⁰Lupoglazoff, N., Rahier, G., Vuillot, F., "Application of the CEDRE Unstructured Flow Solver to Jet Noise Computations," *Proceedings (CD-ROM) of the 1st European Conference for Aerospace Sciences (EUCASS), Moscow, July 4-7, 2005*.
- ¹¹Paliath, U., Morris, P.J., "Prediction of Jet Noise from Circular Beveled Nozzles," *11th AIAA/CEAS Aeroacoustics Conference, 23-25 May 2005, Monterey, California*, AIAA Paper 2005-3096, 2005.
- ¹²Vuillemin, A., Loheac, P., Rahier, G., Vuillot, F., Lupoglazoff, N., "Aeroacoustic Numerical Method Assessment for a Double Stream Nozzle," *11th AIAA/CEAS Aeroacoustics Conference, 23-25 May 2005, Monterey, California*, AIAA Paper 2005-3043, 2005.
- ¹³Strelets, M.Kh., "Detached Eddy Simulation of Massively Separated Flows," *39th AIAA Aerospace Sciences Meeting and Exhibit, 8-11 Jan. 2005, Reno, Nevada*, AIAA Paper 2001-0879, 2001.
- ¹⁴Roe, P.L., "Approximate Riemann Solvers, Parameter Vectors and Difference Schemes," *Journal of Computational Physics*, Vol. 46, 1981, pp. 357-378.
- ¹⁵Van Albada, G.D., Van Leer, B., Roberts, W.W., "A Comparative Study of Computational Methods in Cosmic Gas Dynamics," *Astron. Astrophysics*, Vol. 108, 1982, pp. 76-84.
- ¹⁶Tanna, H.K., "An Experimental Study of Jet Noise. Part II: Shock Associated Noise," *Journal of Sound and Vibration*, Vol. 50, 1977, pp. 429-444.
- ¹⁷Hill, D.J., Pullin, D.I., "Hybrid Tuned Center-Difference-WENO Method for Large Eddy Simulation in the Presence of Strong Shocks," *Journal of Computational Physics*, Vol. 194, 2004, pp. 435-450.
- ¹⁸Shur, M.L., Spalart, P.R., Strelets, M.Kh., "Numerical Approach to the Aeroacoustics of Complex Jet Flows: Methodology, Tests, and Applications," *Proceedings (CD-ROM) of the 1st European Conference for Aerospace Sciences (EUCASS), Moscow, July 4-7, 2005*.
- ¹⁹Viswanathan, K., Shur, M.L., Spalart, P.S., Strelets, M.Kh., "Numerical Prediction of Noise from Round and Beveled Nozzles," *Proc. of Euromech Colloquium 467: "Turbulent Flow and Noise Generation", Marseille, France, 18-20 July, 2005*, <http://www.iag.uni-stuttgart.de/Euromech-467>.
- ²⁰Engquist, B., Majda, A., "Absorbing Boundary Conditions for the Numerical Simulations of Waves," *Mathematics of Computation*, Vol. 31, 1977, pp. 629-651.
- ²¹Viswanathan, K., "Nozzle Shaping for Reduction of Jet Noise from Single Jets," *AIAA Journal*, Vol. 43, No. 5, 2005, pp. 1008-1022.
- ²²Viswanathan, K., "Parametric Study of Noise from Dual-Stream Nozzles," *Journal of Fluid Mechanics*, Vol. 521, 2004, pp. 35-68.
- ²³Viswanathan, K., "An Elegant Concept for Reduction of Jet Noise from Turbofan Engines," *10th AIAA/CEAS Aeroacoustics Conference, 10-12 May 2004, Manchester, UK*, AIAA Paper 2004-2975, 2004.
- ²⁴Papamoschou, D., "New Method for Jet Noise Reduction in Turbofan Engines," *AIAA Journal*, Vol. 42, No. 11, 2004, pp. 2245-2253.
- ²⁵Bridges, J., Brown, C.A., "Parametric Testing of Chevrons on Single Flow Hot Jets," *10th AIAA/CEAS Aeroacoustics Conference, 10-12 May 2004, Manchester, UK*, AIAA Paper 2004-2824, 2004.